Improving PARSEC models for very low mass stars

Yang Chen,[1,2]⋆ Léo Girardi,[3] Alessandro Bressan,[1] Paola Marigo,[4] Mauro Barbieri[4] and Xu Kong[2,5]

[1] *SISSA, via Bonomea 265, I-34136 Trieste, Italy*
[2] *Department of Astronomy, University of Science and Technology of China, Hefei, Anhui 230026, China*
[3] *Osservatorio Astronomico di Padova – INAF, Vicolo dell'Osservatorio 5, I-35122 Padova, Italy*
[4] *Dipartimento di Fisica e Astronomia, Università di Padova, Vicolo dell'Osservatorio 2, I-35122 Padova, Italy*
[5] *Key Laboratory for Research in Galaxies and Cosmology, USTC, Chinese Academy of Sciences, Hefei 230026, China*

ABSTRACT

Many stellar models present difficulties in reproducing basic observational relations of very low mass stars (VLMS), including the mass–radius relation and the optical colour–magnitudes of cool dwarfs. Here, we improve PARSEC (PAdova-TRieste Stellar Evolution Code) models on these points. We implement the T–τ relations from PHOENIX BT-Settl model atmospheres as the outer boundary conditions in the PARSEC code, finding that this change alone reduces the discrepancy in the mass–radius relation from 8 to 5 per cent. We compare the models with multiband photometry of clusters Praesepe and M67, showing that the use of T–τ relations clearly improves the description of the optical colours and magnitudes. But anyway, using both Kurucz and PHOENIX model spectra, model colours are still systematically fainter and bluer than the observations. We then apply a shift to the above T–τ relations, increasing from 0 at $T_{\rm eff}$ = 4730 K to ∼14 per cent at $T_{\rm eff}$ = 3160 K, to reproduce the observed mass–radius relation of dwarf stars. Taking this experiment as a calibration of the T–τ relations, we can reproduce the optical and near-infrared colour–magnitude diagrams of low-mass stars in the old metal-poor globular clusters NGC 6397 and 47 Tuc, and in the intermediate-age and young solar-metallicity open clusters M67 and Praesepe. Thus, we extend PARSEC models using this calibration, providing VLMS models more suitable for the lower main-sequence stars over a wide range of metallicities and wavelengths. Both sets of models are available on PARSEC webpage.

Key words: stars: evolution – Hertzsprung–Russell and colour–magnitude diagrams – stars: low-mass.

1 INTRODUCTION

Very low mass stars (VLMS; $M \lesssim 0.6\,{\rm M_\odot}$) are by far the most numerous stars in the Galaxy. For a Kroupa (2001) or Chabrier (2001) initial mass function, they constitute about 1/3 of the formed stars. Contrarily to the more massive stars, they remain burning hydrogen during the entire Hubble time, being observable at about the same luminosities from the moment they settle on the main sequence (MS) up to very old ages. At the near-solar metallicities that characterize the solar neighbourhood, they appear mostly as M dwarfs, with their spectral energy distribution (SED) peaking at near-infrared wavelengths and marked by numerous molecular bands of TiO, VO, water vapour, etc. (see e.g. Allard & Hauschildt 1995; Allard et al. 1997). At the lower metallicities typical of the thick disc and halo, they also appear as K dwarfs, with their SEDs peaking at red wavelengths (*R* and *I* bands).

VLMS appear copious in *any* deep imaging survey of the Galaxy [such as Sloan Digital Sky Survey (SDSS) and Dark Energy Survey (DES)], and even more in infrared imaging campaigns such as 2MASS (Skrutskie et al. 2006), UKIRT Infrared Deep Sky Survey (UKIDSS) (Lawrence et al. 2007), European Southern Observatory (ESO)/Visible and Infrared Survey Telescope for Astronomy (VISTA) public surveys (Arnaboldi et al. 2012) and *WISE* (Wright et al. 2010). Suffice it to mention that almost half of the 2MASS point sources (Cutri et al. 2003) concentrate at $J - K_{\rm s} \simeq 0.85$, in a sort of *vertical finger* in near-infrared colour–magnitude diagrams (CMDs; e.g. Nikolaev & Weinberg 2000); this finger is dominated by M dwarfs at magnitudes $K_{\rm s} \gtrsim 14$, except at very low galactic latitudes (Zasowski et al. 2013). In the optical, instead, VLMS appear along well-defined colour–magnitude relations, as indicated by stars in open clusters, that made them amenable for the distance derivations via photometric parallaxes, and hence valuable probes of the Milky Way structure (Siegel et al. 2002; Jurić et al. 2008; Ivezić, Beers & Jurić 2012).

⋆ E-mail: ychen@sissa.it

VLMS are also frequent among the targets of planet searches. Indeed, almost the totality of *Kepler* planet candidates (95 per cent; cf. Borucki et al. 2011) are found around dwarfs with masses below 1.2 M$_\odot$, with the best chances of finding Earth-mass planets being around the targets of even smaller masses (e.g. Quintana et al. 2014). In the case of transit detection, the presence of a well-defined mass–radius relation (Torres, Andersen & Giménez 2010) allows the easy derivation of planetary properties.

Despite the great importance of the mass–radius relation of VLMS, it has been poorly predicted and badly matched in present grids of stellar models, with models tending to systematically underestimate the stellar luminosity/radii for a given mass (Torres et al. 2010). Significant clarifications have been recently provided by Feiden & Chaboyer (2012) and Spada et al. (2013), who identify the surface boundary conditions in the VLMS models as a critical factor for improving the data–model agreement. Anyway, even for the best models and data, a discrepancy of about 3 per cent remains in the observed radii (Spada et al. 2013). Another recurrent discrepancy is in the colour–magnitude relations of VLMS: indeed, models that fairly well reproduce the near-infrared colours of VLMS in star clusters (as in Sarajedini, Dotter & Kirkpatrick 2009) tend to have optical colours which are far too blue at the bottom of the MS, as indicated in An et al. (2008), and as we will show in the following. A similar discrepancy also appears in low-metallicity globular clusters (e.g. Campos et al. 2013). These disagreements imply that present isochrones cannot be safely used to estimate the absolute magnitudes – and hence distances – of field dwarfs, once their optical colours and apparent magnitudes are measured. Instead, empirical luminosity–colour relations have been preferred for this (e.g. Jurić et al. 2008; Green et al. 2014).

In this paper, we will revise the PAdova-TRieste Stellar Evolution Code (PARSEC; Bressan et al. 2012) seeking for a significant improvement of their VLMS models. The way devised to do so is centred on the revision of the T–τ relation used as the outer boundary condition in stellar models, as will be described in Section 2. The revised VLMS models will be transformed into isochrones and compared to some key observations in Section 3. The improvement in the models is clear, as summarized in Section 4; however, an additional ad hoc correction to the T–τ relation is needed to bring models and data into agreement. A subsequent paper will be devoted to a more thorough discussion of the available model atmospheres and synthetic spectra for M dwarfs.

2 MODELS

2.1 The stellar evolution code

PARSEC is an extended and updated version of the code previously used by Bressan, Chiosi & Bertelli (1981), Girardi et al. (2000) and Bertelli et al. (2008), as thoroughly described by Bressan et al. (2012). The main updates regard

(i) full consideration of pre-MS phases;

(ii) the equation of state (EOS) from FREEEOS v2.2.1 by Alan W. Irwin;[1]

(iii) revised opacities from AESOPUS (Marigo & Aringer 2009)[2] and the OPAL group (Iglesias & Rogers 1996);[3]

(iv) adoption of the revised Caffau et al. (2008, 2009) solar chemical abundances;

(v) extended nuclear networks and the reaction rates recommended in the updated JINA REACLIB Database (Cyburt et al. 2010);[4]

(vi) microscopic diffusion is allowed to operate in low-mass stars;

(vii) the temperature gradient is described by the mixing length theory (Böhm-Vitense 1958), with the parameter $\alpha_{MLT} = 1.74$ being calibrated by means of a solar model which is tested against helioseismologic constraints (Basu et al. 2009).

The code as described in Bressan et al. (2012) still makes use of the grey atmosphere approximation (Mihalas 1978) as the external boundary condition, i.e. the relation between the temperature and Rosseland mean optical depth τ across the atmosphere, T–τ, is given by

$$T^4(\tau) = \frac{3}{4}T_{eff}^4\left[\tau + q(\tau)\right], \tag{1}$$

where $q(\tau) \approx 2/3$ is the Hopf function.

The PARSEC v1.1 release of tracks contains stellar evolutionary models in a wide range of masses down to 0.1 M$_\odot$, with ages from 0 to 15 Gyr, and for several values of metal content going from $Z = 0.0001$ to 0.06.

These are the VLMS tracks we are going to revise. For guidance, Table 1 presents a summary of the main characteristics of these models, and of the other models that will be introduced later in this paper.

2.2 The model atmospheres

Following the indications from various authors (e.g. VandenBerg et al. 2008; Feiden & Chaboyer 2012; Spada et al. 2013), we replace the approximation in equation (1) by the T–τ relations provided by real model atmospheres. We use the large library of model atmospheres from PHOENIX (Allard, Homeier & Freytag 2012, and references therein),[5] and in particular the set of BT-Settl models computed with the Asplund et al. (2009) chemical composition, which contains the most complete coverage in stellar parameters (temperature, gravity and metallicity) for both stellar spectra and atmosphere structures.

The T–τ relations in PHOENIX (BT-Settl) cover the range of $2600 < T_{eff}/K < 700\,000$ and $0.5 < \log g < 6$ (with g in cm s^{-2}), for metallicities Z between ∼0.04 and 0.000 003. They are well behaved and generally cover the entire interval from $\tau = 0$ to $\tau \geq 100$. Fig. 1 shows some selected polynomial fits performed to the atmosphere models, from $\tau = 10^{-4}$ to the boundary at $\tau = 2/3$. They provide an excellent representation of the T–τ data. The polynomial fits are obtained for each metallicity, T_{eff} and $\log g$ in the data base, and later interpolated among these three parameters.

PARSEC solves the stellar structure at each time step via the Henyey, Forbes & Gould (1964) method as described in Hofmeister, Kippenhahn & Weigert (1964) and Kippenhahn, Weigert & Weiss (2013). In the atmosphere integration, the family of T–τ relations – written as a function of T_{eff}, $\log g$ and [Fe/H] – replace the simple surface boundary condition formerly represented by equation (1) in the following way: the boundary is set at $\tau' = 2/3$. The pressure P is integrated starting from the radiative pressure value at $\tau = 0$ up to

---

Table 1. Summary of the PARSEC models for VLMS discussed in this paper.

| Model	BC	T–τ	BC tables used for VLMS	Basic description
v1.1	OBC	Grey atmosphere	Castelli & Kurucz (2003) and Allard et al. (2000)	Previous version of PARSEC models and BC tables
v1.1	NBC	Grey atmosphere	Castelli & Kurucz (2003) + PHOENIX BT-Settl	PARSEC v1.1 models interpolated with our new BC tables
v1.2	NBC	PHOENIX BT-Settl	Castelli & Kurucz (2003) + PHOENIX BT-Settl	New VLMS models with T–τ relation from PHOENIX BT-Settl
v1.2S	NBC	Calibrated PHOENIX BT-Settl	Castelli & Kurucz (2003) + PHOENIX BT-Settl	New VLMS models with calibrated T–τ relation with respect to PHOENIX BT-Settl
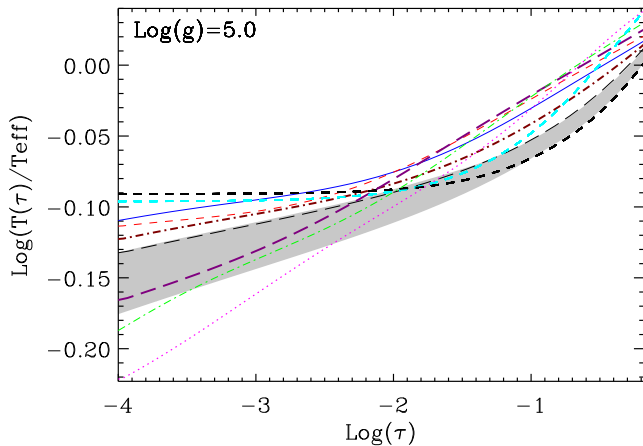
Figure 1. A family of polynomial fits to the T–τ relations from PHOENIX (BT-Settl), for [Fe/H] = 0 and log g = 5.0, in the region from $\tau = 10^{-4}$ to 2/3. All T–τ curves have been divided by $T_{\rm eff}$ so as to reduce the vertical scale in the plot. The magenta dot, green dash–dotted, purple thick long dashed, red dashed, blue solid, brown thick dash–dotted and black long dashed curves are for $T_{\rm eff}$/K = 2600, 2800, 3000, 3500, 4000, 4300 and 4700, respectively. For $4700 < T_{\rm eff}/{\rm K} \leq 10\,000$, we show only the area occupied by the models (grey shaded). Other relations useful for the discussion in this paper are also presented: the Krishna Swamy (1966) relation (cyan thick dashed line) and the grey atmosphere approximation as in equation (1) (black thick dashed line).

its value at τ' via $d\tau/dP = \kappa R^2/GM$, where κ is the Rosseland mean opacity, R and M are the stellar radius and total mass, and G is the gravitational constant.

2.3 The role of bolometric corrections

PHOENIX BT-Settl atmosphere models provide not only the T–τ relations to be used as the external boundary conditions, but also an extended grid of synthetic SEDs from which we can compute bolometric correction (BC_λ) tables. We have also implemented the new BC tables to convert the basic output of stellar models into the absolute magnitudes in several passbands M_λ, with

$$M_\lambda = M_{\rm bol} - BC_\lambda, \qquad (2)$$

where $M_{\rm bol} = -2.5\log (L/{\rm L_\odot}) - 4.7554$. The formalism to compute BC_λ is thoroughly described in Girardi et al. (2002), and will not be repeated here. Suffice it to recall that it depends primarily on $T_{\rm eff}$, and to a lesser extent also on surface gravity and metallicity.

These tables of BC_λ will be used later in this paper, for the $T_{\rm eff}$ interval between 2600 and 6000 K, as an alternative to the previous tables used in PARSEC – which were based on Castelli & Kurucz (2003) and Allard et al. (2000) model atmospheres. In the

following, new BC tables will be referred to as NBC, while the previous ones as OBC (see Table 1). As we will discuss later, the new BC have a significant role mainly in the near-infrared colours.

2.4 The new VLMS models

We follow the same procedure as described in Bressan et al. (2012) to calibrate the solar model using the new T–τ relations. The new solar model has $\alpha_{\rm MLT} = 1.77$, which is slightly higher than the previous one used for PARSEC v1.1 (namely $\alpha_{\rm MLT} = 1.74$; see Bressan et al. 2012). We have recomputed VLMS models using the new T–τ relations and $\alpha_{\rm MLT} = 1.77$, for all compositions contained in the previous PARSEC v1.1 release, giving origin to PARSEC v1.2 tracks. They start at the birth line defined by a central temperature of 5×10^4 K, evolve through the pre-MS where the main stages of D and ^{3}He burning occur, and finally settle on the zero-age main sequence (ZAMS). Evolution in the MS is quite slow and takes longer than 15 Gyr for all masses smaller than about 1 M$_\odot$.

It is evident from the mass–radius relation of Fig. 2 and the $\log L$ versus $\log T_{\rm eff}$ panels of Figs 3–6 (and discussions later in Section 3) that the use of the new T–τ relation has a significant impact on the stellar radii and on the shape of the lower MS, with the new ZAMS models becoming significantly larger, cooler (by up to $\Delta T_{\rm eff} \simeq 200$ K) and slightly less luminous, for model stars of the same mass (look at the difference between black and blue lines in Fig. 2, and between blue and green curves in Figs 3–6). In the Hertzsprung–Russell (H–R) diagrams, however, the lower ZAMS does never become as straight as the upper MS. As clarified long ago by Copeland, Jensen & Jorgensen (1970), the curved shape of the lower MS is mainly due to the changes in the EOS, which enters into a range of significantly higher densities for VLMS. Particularly important are the roles of Coulomb interactions and the formation of the H$_2$ molecule, which causes a strong reduction of the adiabatic temperature gradient, $\nabla_{\rm ad} = (\partial \log T/\partial \log P)_S$, from 0.4 to about 0.1, in the outer layers of the coolest dwarfs.

3 COMPARISON WITH THE DATA

In this section, we compare the models with a few, selected observational data sets. We start with the mass–radius relation because it is a fundamental relation that does not involve the stellar SEDs. Then, we discuss the observed CMDs of two open clusters (Praesepe and M67, representing solar metallicity) and two globular clusters (47 Tuc and NGC 6397, representing metal poor environments).

3.1 The mass–radius relation

Fig. 2 shows the mass–radius relation derived from our tracks, as compared with recent observational data for nearby stars, obtained
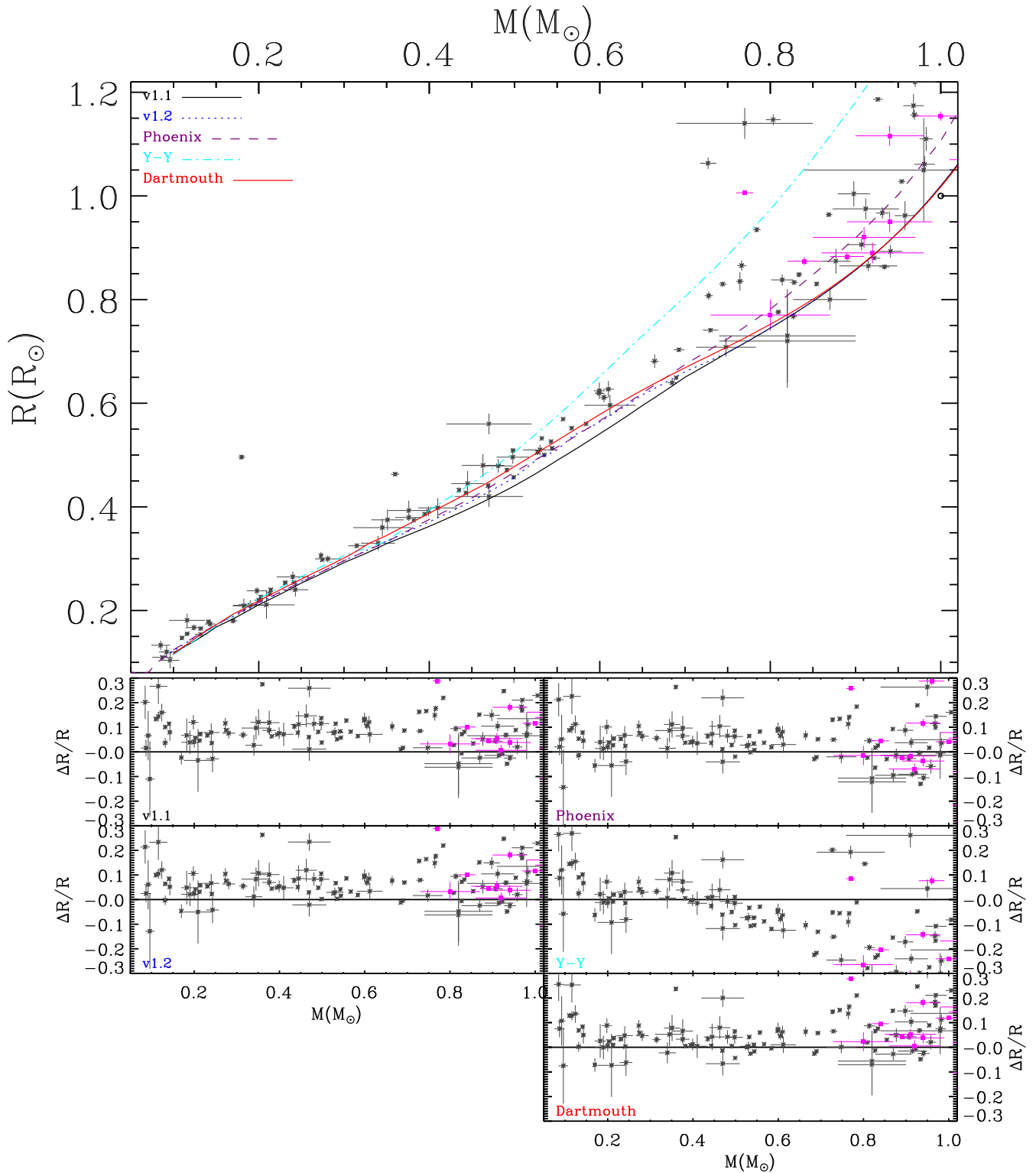
Figure 2. The empirical mass–radius relation for low-mass stars in the solar neighbourhood using compiled data listed in Table 2. Black asterisks are binary stars; magenta squares are single stars. In the upper-left panel, isochrones of 5 Gyr are overplotted for comparison for different models. PARSEC v1.1 isochrones are shown in black, while our updated isochrones (v1.2, $Z = 0.02$) are in blue. PHOENIX ($Z = 0.02$), Y–Y ($Z = 0.016\,31$) and Dartmouth ($Z = 0.018\,85$) models are in purple, cyan and red, respectively. The other panels are the differences compared to the observation for different models as the labels shown. The Y-axis of $\Delta R/R$ is defined as $(R_{\mathrm{obs}} - R_{\mathrm{mod,\,5\,Gyr}})/R_{\mathrm{obs}}$.
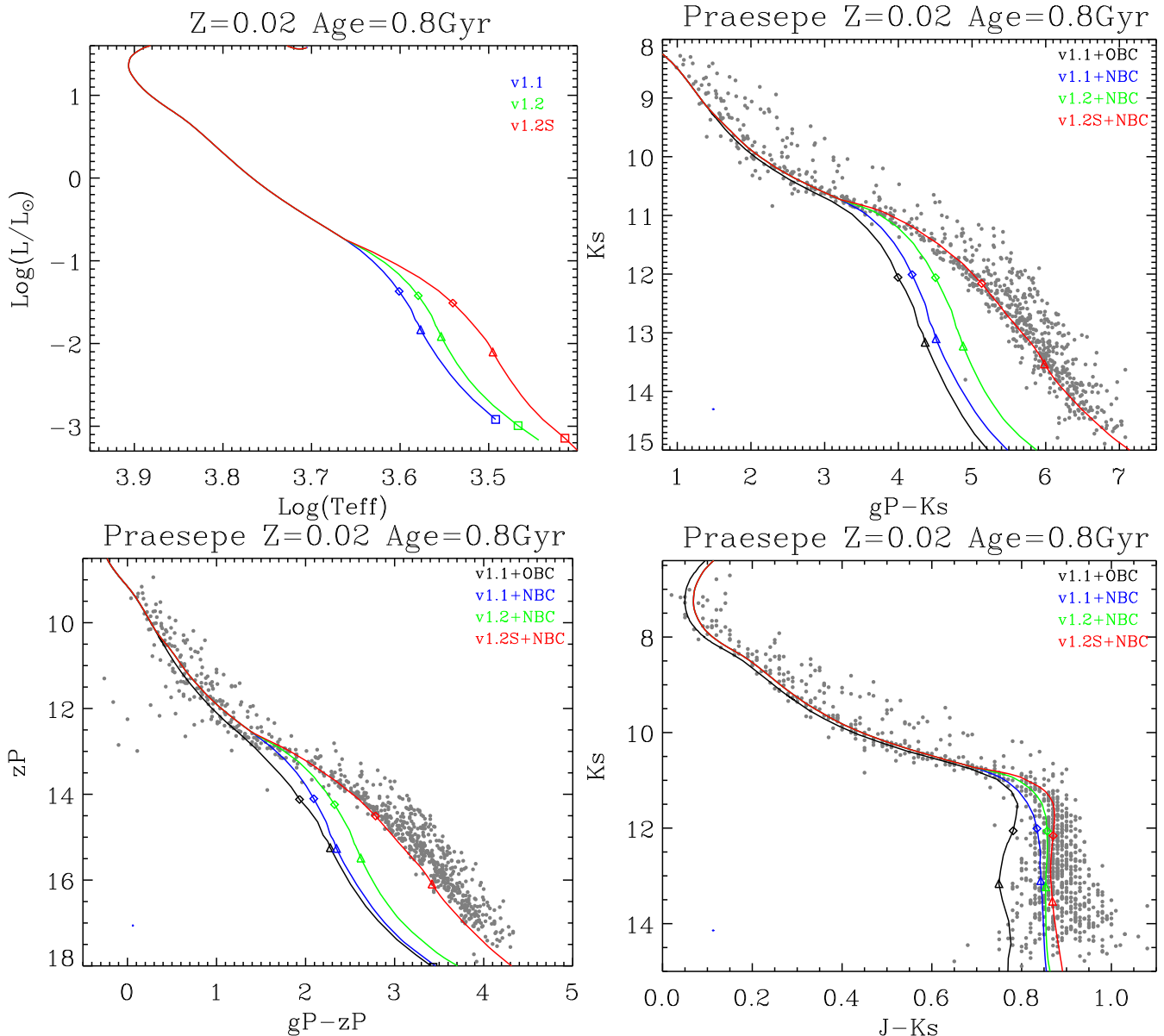
Figure 3. CMDs for Praesepe. The data points come from Wang et al. (2014) with Pan-STARRS and 2MASS data. Black curves: PARSEC v1.1 isochrones with our previous BC tables; blue curves: PARSEC v1.1 isochrones with new BC tables; green curves: new isochrones (v1.2) with $T-\tau$ relation derived from PHOENIX (BT-Settl) models and interpolated with new BC tables; red curves: new isochrones (v1.2S) with calibrated $T-\tau$ relation upon those derived from PHOENIX (BT-Settl) models and interpolated with new BC tables. The galactic reddening we use for Praesepe is $E(B-V) = 0.01$ and the distance modulus is $(m - M)_0 = 6.30$ mag (from *Hipparcos* parallaxes; van Leeuwen 2009). The isochrones are for $Z = 0.02$ and age $= 0.8$ Gyr. We also indicate the initial masses of 0.5, 0.3, 0.1 $M_\odot$ along the isochrones with open diamonds, triangles and squares, respectively.

either via asteroseismic techniques, or via eclipsing binaries.[6] The full data set is presented in Table 2. Among these observations, the most direct ones are likely those from the eclipsing binaries (see Torres et al. 2010; Kraus et al. 2011), since they do not depend on any suspicious assumption or uncertain empirical calibration between the photometry and $T_{\rm eff}$. The same happens for the few eclipsing binaries in which the primary is a white dwarf, taken from

Parsons et al. (2012a,b), in which the M dwarf masses and radii are particularly well constrained.[7]

It is obvious that the PARSEC v1.1 mass–radius relation is systematically below the empirical data, with a typical deficit of 8 per cent in the radius for a given mass, over the entire interval between 0.1

---

[6] Stars measured via interferometric techniques are discarded, since their masses are derived using either empirical or theoretical mass–luminosity relations.

[7] The situation essentially does not change if we adopt the recent compilation of masses and radii from Eker et al. (2014), which however is less complete for masses smaller than 0.4 $M_\odot$, and does not contain any star below 0.18 $M_\odot$. While in this paper we pay more attention to the lower masses, we decide to just use our own collected data.
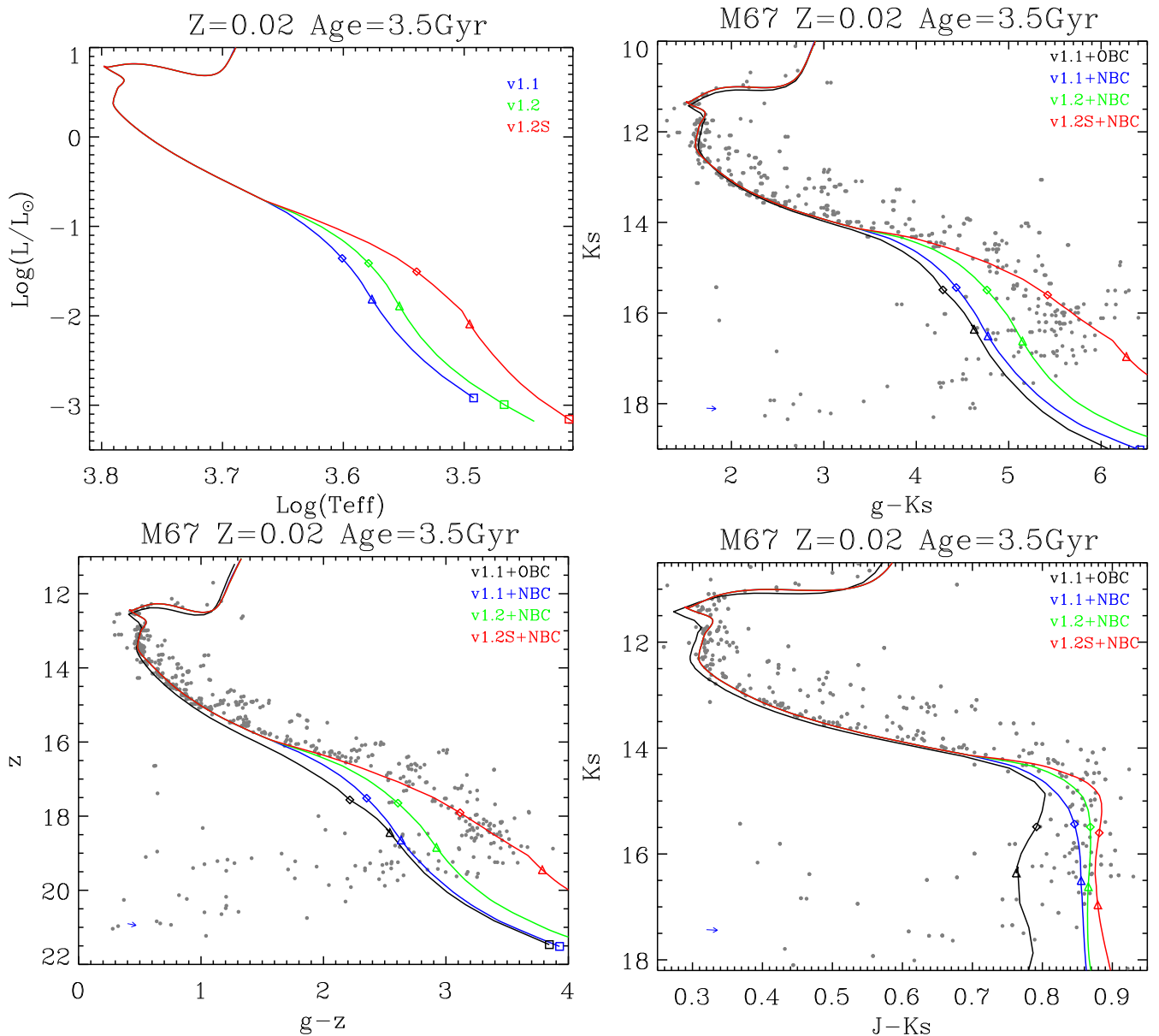
Figure 4. M67 in several CMDs. The data points come from matching Yadav et al. (2008) catalogue with SDSS and 2MASS catalogues (see the text). The labels are the same as in Fig. 3. The blue arrow in the lower-left corner of each panel is the reddening vector. The galactic reddening we use for M67 is $E(B - V) = 0.03$ and the distance modulus is $(m - M)_0 = 9.75$ mag. The isochrones are for $Z = 0.02$ and age = 3.5 Gyr.

and 0.7 $M_\odot$. For masses higher than $\sim$0.7 $M_\odot$, the comparison between model and observed radii is not very significant since the radii increase with the stellar age, so that both models and observations tend to occupy a wider range in this parameter.

This mismatch in the stellar radii is very significant, and has already been noticed by a number of authors (e.g. Casagrande, Flynn & Bessell 2008; Kraus et al. 2011, and references therein). It has inspired a few alternative explanations, for instance an additional growth in radius caused by rotation (Irwin et al. 2011; Kraus et al. 2011) and magnetic fields (e.g. Spruit & Weiss 1986; Feiden & Chaboyer 2012, 2013; MacDonald & Mullan 2013; Jackson & Jeffries 2014, and references therein). These mechanisms may indicate that eclipsing binaries follow a different mass–radius relation than single field stars, although Boyajian et al. (2012) and Spada et al. (2013) find that their radii are indistinguishable.

The lower-left panel of Fig. 2 shows that in PARSEC v1.2 models, this mismatch is reduced down to $\sim$5 per cent.

We verified that it is really hard to eliminate this discrepancy in radii. For a few tracks, we have explored a change in the EOS, testing for instance the use of our previous Mihalas et al. (1990) EOS for temperatures lower than 10^7 K, and the OPAL EOS (Rogers, Swenson & Iglesias 1996) for higher temperatures. The effect on the radii was close to null. Moreover, we note that our adopted FREEEOS is a modern EOS that includes all major effects of relevance here. We note in particular that our models reproduce the velocity of sound across the Sun to within 0.6 per cent, which is well within the error bars. Therefore, the situation is not easily remediable: significant changes in the EOS, apart from not being motivated, would probably ruin the agreement with the standard solar model.
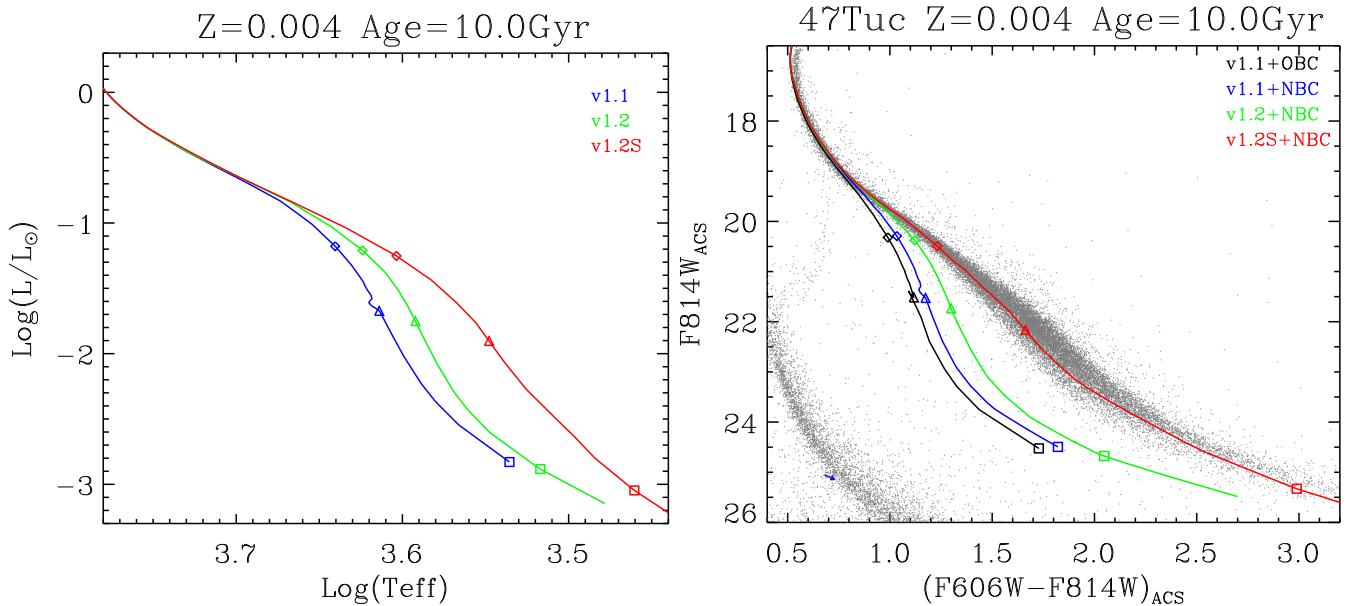
Figure 5. CMDs for 47 Tuc. The data points are from Kalirai et al. (2012). The sequences at the bottom-left corner of the CMD correspond to the background SMC population and should be ignored. Model isochrones are presented with the same labels as in Fig. 3, but for a reddening of $E(B - V) = 0.05$ mag, and a distance modulus of $(m - M)_0 = 13.20$ mag. The isochrones are for $Z = 0.004$ and an age of 10 Gyr.
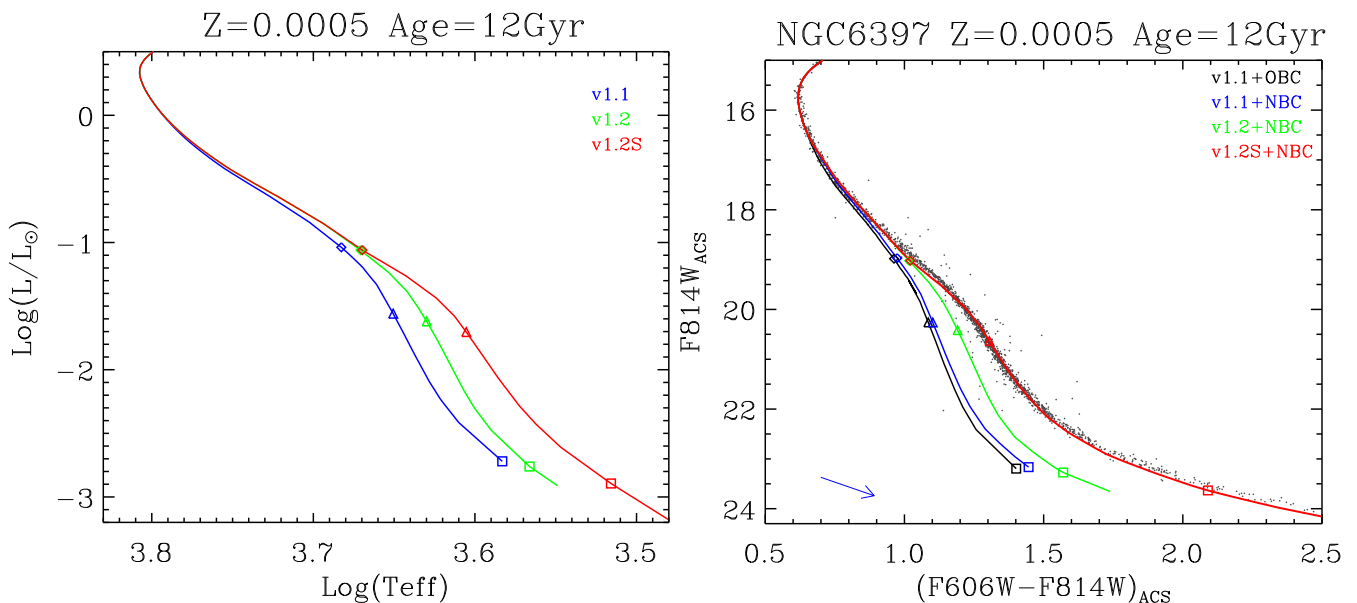

Figure 6. CMDs for NGC 6397. The data points come from Richer et al. (2008). Model isochrones are presented with the same labels as in Fig. 3, but for a reddening of $E(B - V) = 0.2$ mag, and a distance modulus of $(m - M)_0 = 11.95$ mag. The isochrones are for $Z = 0.0005$ and an age of 12 Gyr.

Changes in the mixing-length parameter α_{MLT} also revealed to be non-influential: models with α_{MLT} as low as 0.1 have their radii increased by only ∼2 per cent. The use of very different metallicities and helium contents does not change the situation either.

Fig. 2 also compares the mass–radius data with three other recent sets of models.

(i) 'PHOENIX', which are essentially the Baraffe et al. (1997, 1998) theoretical isochrones transformed with their synthetic colour tables. They have not implemented their T–τ relation into their isochrones, but only the colours.

(ii) Yale–Yonsei (Y–Y; Spada et al. 2013) which used PHOENIX (BT-Settl) T–τ relation to improve their previous Y–Y models. $\alpha_{MLT} = 1.743$ was used. They demonstrate the large improvement compared to their previous models for masses below 0.6 $M_\odot$.

(iii) Dartmouth (Dotter et al. 2008) which used PHOENIX model atmospheres (both T–τ and the synthetic colour–T_{eff} transformations) and $\alpha_{MLT} = 1.938$.

All models are computed for metallicities close to solar. It is easy to notice that PHOENIX models present almost the same discrepancy as ours, for the entire mass range of VLMS. Dartmouth models present more or less the same pattern, but with reduced discrepancies in the

Table 2. Mass–radius data. Notations used are AS: asteroseismic; SYN: spin–orbit synchronization; SB1: single-lined binary; EH: exoplanet host. 2MASS04463285: 2MASS04463285+1901432. LP133-373: mass ratio = 1 assumed.

Name	$M_*(\mathrm{M_\odot})$	$\sigma(M_*(\mathrm{M_\odot}))$	$R_*(\mathrm{R_\odot})$	$\sigma(R_*(\mathrm{R_\odot}))$	System type	Method	Ref.[a]	Comment
KIC6521045	1.08	±0.06	1.49	±0.04	Single	AS	[1]	EH
KIC3544595	0.91	±0.06	0.92	±0.02	Single	AS	[1]	EH
KIC4914423	1.09	±0.07	1.44	±0.04	Single	AS	[1]	EH
KIC8349582	1.08	±0.08	1.41	±0.04	Single	AS	[1]	EH
KIC5094751	1.04	±0.06	1.32	±0.04	Single	AS	[1]	EH
KIC4349452	1.19	±0.06	1.31	±0.02	Single	AS	[1]	EH
KIC8478994	0.80	±0.07	0.77	±0.03	Single	AS	[1]	EH
KIC11295426	1.08	±0.05	1.24	±0.02	Single	AS	[1]	EH
KIC8753657	1.07	±0.06	1.07	±0.02	Single	AS	[1]	EH
KIC10963065	1.08	±0.07	1.23	±0.03	Single	AS	[1]	EH
KIC9955598	0.92	±0.06	0.89	±0.02	Single	AS	[1]	EH
TrES-2	0.94	±0.05	0.95	±0.02	Single	RV	[2]	EH
HATS550-016_P	0.97	$^{+0.05}_{-0.06}$	1.22	$^{+0.02}_{-0.03}$	Binary	SYN	[3]	SB1
HATS550-016_S	0.110	$^{+0.005}_{-0.006}$	0.147	$^{+0.003}_{-0.004}$	Binary	SYN	[3]	SB1
HATS551-019_P	1.10	$^{+0.05}_{-0.09}$	1.70	$^{+0.09}_{-0.09}$	Binary	SYN	[3]	SB1
HATS551-019_S	0.17	$^{+0.01}_{-0.01}$	0.18	$^{+0.01}_{-0.01}$	Binary	SYN	[3]	SB1
HATS551-021_P	1.1	$^{+0.1}_{-0.1}$	1.20	$^{+0.08}_{-0.01}$	Binary	SYN	[3]	SB1
HATS551-021_S	0.132	$^{+0.014}_{-0.005}$	0.154	$^{+0.006}_{-0.008}$	Binary	SYN	[3]	SB1
HATS553-001_P	1.2	$^{+0.1}_{-0.1}$	1.58	$^{+0.08}_{-0.03}$	Binary	SYN	[3]	SB1
HATS553-001_S	0.20	$^{+0.01}_{-0.02}$	0.22	$^{+0.01}_{-0.01}$	Binary	SYN	[3]	SB1
HP_Aur_P	0.9543	±0.0041	1.0278	±0.0042	Binary	RV	[4]	
HP_Aur_S	0.8094	±0.0036	0.7758	±0.0034	Binary	RV	[4]	
V65_P	0.8035	±0.0086	1.1470	±0.0104	Binary	RV	[5]	
V65_S	0.6050	±0.0044	0.6110	±0.0092	Binary	RV	[5]	
V66_P	0.7842	±0.0045	0.9347	±0.0048	Binary	RV	[5]	
V66_S	0.7443	±0.0042	0.8298	±0.0053	Binary	RV	[5]	
V69_P	0.7665	±0.0053	0.8655	±0.0097	Binary	RV	[5]	
V69_S	0.7278	±0.0048	0.8074	±0.0080	Binary	RV	[5]	
HD181068_A	3.0	±0.1	12.46	±0.15	Triple	RV	[6]	
HD181068_Ba	0.915	±0.034	0.865	±0.010	Triple	RV	[6]	
HD181068_Bb	0.870	±0.043	0.800	±0.020	Triple	RV	[6]	
C4780Bb	0.096	±0.011	0.104	±0.0160	Binary	RV	[7]	Primary:F-star
NSVS07394765_P	0.360	±0.005	0.463	±0.004	Binary	RV	[8]	
NSVS07394765_S	0.180	±0.004	0.496	±0.005	Binary	RV	[8]	
WTS19g-4-02069_P	0.53	±0.02	0.51	±0.01	Binary	RV	[9]	
WTS19g-4-02069_S	0.143	±0.006	0.174	±0.006	Binary	RV	[9]	
KOI-126A	1.3470	±0.0320	2.0254	±0.0098	Triple	RV	[10]	
KOI-126B	0.2413	±0.0030	0.2543	±0.0014	Triple	RV	[10]	
KOI-126C	0.2127	±0.0026	0.2318	±0.0013	Triple	RV	[10]	
KIC6131659_P	0.922	±0.007	0.8800	±0.0028	Binary	RV	[11]	
KIC6131659_S	0.685	±0.005	0.6395	±0.0061	Binary	RV	[11]	
MG1-78457_P	0.527	±0.002	0.505	$^{+0.008}_{-0.007}$	Binary	RV	[12]	
MG1-78457_S	0.491	±0.001	0.471	$^{+0.009}_{-0.007}$	Binary	RV	[12]	
MG1-116309_P	0.567	±0.002	0.552	$^{+0.004}_{-0.013}$	Binary	RV	[12]	
MG1-116309_S	0.532	±0.002	0.532	$^{+0.004}_{-0.008}$	Binary	RV	[12]	
MG1-506664_P	0.584	±0.002	0.560	$^{+0.001}_{-0.004}$	Binary	RV	[12]	
MG1-506664_S	0.544	±0.002	0.513	$^{+0.001}_{-0.008}$	Binary	RV	[12]	
MG1-646680_P	0.499	±0.002	0.457	$^{+0.006}_{-0.004}$	Binary	RV	[12]	
MG1-646680_S	0.443	±0.002	0.427	$^{+0.006}_{-0.002}$	Binary	RV	[12]	
MG1-1819499_P	0.557	±0.001	0.569	$^{+0.002}_{-0.023}$	Binary	RV	[12]	
MG1-1819499_S	0.535	±0.001	0.500	$^{+0.003}_{-0.014}$	Binary	RV	[12]	
MG1-2056316_P	0.469	±0.002	0.441	$^{+0.002}_{-0.002}$	Binary	RV	[12]	
MG1-2056316_S	0.382	±0.001	0.374	$^{+0.002}_{-0.002}$	Binary	RV	[12]	
SDSSJ12120123	0.273	±0.002	0.306	±0.007	Binary	RV	[13]	Primary:WD
GK-Vir	0.116	±0.003	0.155	±0.003	Binary	RV	[13]	Primary:WD
SDSSJ0857+0342	0.087	±0.012	0.1096	±0.0038	Binary	RV	[14]	Primary:WD
SDSS01380016	0.132	±0.003	0.165	±0.001	Binary	RV	[15]	Primary:WD
Kepler-16_P	0.6897	$^{+0.0035}_{-0.0034}$	0.6489	$^{+0.0013}_{-0.0013}$	Binary	RV	[16]	
Kepler-16_S	0.202 55	$^{+0.000 66}_{-0.000 654}$	0.226 23	$^{+0.000 59}_{-0.000 53}$	Binary	RV	[16]	
CM-Dra_P	0.2310	±0.0009	0.2534	±0.0019	Binary	RV	[17]	
CM-Dra_S	0.2141	±0.0010	0.2396	±0.0015	Binary	RV	[17]	
T-Boo0-00080_P	1.49	±0.07	1.83	±0.03	Binary	SYN	[18]	

Table 2 – *continued*

Name	$M_*(\mathrm{M}_\odot)$	$\sigma(M_*(\mathrm{M}_\odot))$	$R_*(\mathrm{R}_\odot)$	$\sigma(R_*(\mathrm{R}_\odot))$	System type	Method	Ref.[a]	Comment
T-Boo0-00080_S	0.315	±0.010	0.325	±0.005	Binary	SYN	[18]	
T-Lyr1-01662_P	0.77	±0.08	1.14	±0.03	Binary	SYN	[18]	
T-Lyr1-01662_S	0.198	±0.012	0.238	±0.007	Binary	SYN	[18]	
T-Lyr0-08070_P	0.95	±0.11	1.36	±0.05	Binary	SYN	[18]	
T-Lyr0-08070_S	0.240	±0.019	0.265	±0.010	Binary	SYN	[18]	
T-Cyg1-01385_P	0.91	±0.15	1.63	±0.08	Binary	SYN	[18]	
T-Cyg1-01385_S	0.345	±0.034	0.360	±0.017	Binary	SYN	[18]	
HAT-TR-205-013_P	1.04	±0.13	1.28	±0.04	Binary	RV	[19]	SB1
HAT-TR-205-013_S	0.124	±0.010	0.167	±0.006	Binary	RV	[19]	SB1
ASAS-01A_P	0.612	±0.030	0.596	±0.020	Multiple	RV	[20]	
ASAS-01A_P	0.445	±0.019	0.445	±0.024	Multiple	RV	[20]	
LSPM-J1112+7626_P	0.3946	±0.0023	0.3860	$^{+0.0055}_{-0.0028}$	Binary	RV	[21]	
LSPM-J1112+7626_S	0.2745	±0.0012	0.2978	$^{+0.0049}_{-0.0046}$	Binary	RV	[21]	
WTS19b-2-01387_P	0.498	±0.019	0.496	±0.013	Binary	RV	[22]	
WTS19b-2-01387_S	0.481	±0.017	0.479	±0.013	Binary	RV	[22]	
WTS19c-3-01405_P	0.410	±0.023	0.398	±0.019	Binary	RV	[22]	
WTS19c-3-01405_S	0.376	±0.024	0.393	±0.019	Binary	RV	[22]	
WTS19e-3-08413_P	0.463	±0.025	0.480	±0.022	Binary	RV	[22]	
WTS19e-3-08413_S	0.351	±0.019	0.375	±0.020	Binary	RV	[22]	
V1061-Cyg_P	1.282	±0.016	1.616	±0.017	Binary	RV	[23]	
V1061-Cyg_S	0.9315	±0.0074	0.967	±0.011	Binary	RV	[23]	
RT-And_P	1.240	±0.030	1.256	±0.015	Binary	RV	[23]	
RT-And_S	0.907	±0.017	0.906	±0.011	Binary	RV	[23]	
FL-Lyr_P	1.218	±0.016	1.283	±0.028	Binary	RV	[23]	
FL-Lyr_S	0.958	±0.012	0.962	±0.028	Binary	RV	[23]	
ZZ-UMa_P	1.1386	±0.0052	1.513	±0.019	Binary	RV	[23]	
ZZ-UMa_S	0.9691	±0.0048	1.1562	±0.0096	Binary	RV	[23]	
α-Cen_P	1.105	±0.007	1.224	±0.003	Binary	RV	[23]	
α-Cen_S	0.934	±0.006	0.863	±0.005	Binary	RV	[23]	
V568-Lyr_P	1.0745	±0.0077	1.400	±0.016	Binary	RV	[23]	
V568-Lyr_S	0.8273	±0.0042	0.7679	±0.0064	Binary	RV	[23]	
V636Cen_P	1.0518	±0.0048	1.0186	±0.0043	Binary	RV	[23]	
V636Cen_S	0.8545	±0.0030	0.8300	±0.0043	Binary	RV	[23]	
CV-Boo_P	1.032	±0.013	1.263	±0.023	Binary	RV	[23]	
CV-Boo_S	0.968	±0.012	1.174	±0.023	Binary	RV	[23]	
V1174-Ori_P	1.006	±0.013	1.338	±0.011	Binary	RV	[23]	
V1174-Ori_S	0.7271	±0.0096	1.063	±0.011	Binary	RV	[23]	
UV-Psc_P	0.9829	±0.0077	1.110	±0.023	Binary	RV	[23]	
UV-Psc_S	0.7644	±0.0045	0.835	±0.018	Binary	RV	[23]	
CG-Cyg_P	0.941	±0.014	0.893	±0.012	Binary	RV	[23]	
CG-Cyg_S	0.814	±0.013	0.838	±0.011	Binary	RV	[23]	
RW-Lac_P	0.9263	±0.0057	1.1864	±0.0038	Binary	RV	[23]	
RW-Lac_S	0.8688	±0.0040	0.9638	±0.0040	Binary	RV	[23]	
HS-Aur_P	0.898	±0.019	1.004	±0.024	Binary	RV	[23]	
HS-Aur_S	0.877	±0.017	0.874	±0.024	Binary	RV	[23]	
GU-Boo_P	0.6101	±0.0064	0.627	±0.016	Binary	RV	[23]	
GU-Boo_S	0.5995	±0.0064	0.624	±0.016	Binary	RV	[23]	
YY-Gem_P	0.5992	±0.0047	0.6194	±0.0057	Binary	RV	[23]	
YY-Gem_S	0.5992	±0.0047	0.6194	±0.0057	Binary	RV	[23]	
CU-Cnc_P	0.4349	±0.0012	0.4323	±0.0055	Binary	RV	[23]	
CU-Cnc_S	0.399 22	±0.000 89	0.3916	±0.0094	Binary	RV	[23]	
CM-Dra_P	0.231 02	±0.000 89	0.2534	±0.0019	Binary	RV	[23]	
CM-Dra_S	0.214 09	±0.000 83	0.2398	±0.0018	Binary	RV	[23]	
LP133-373	0.34	±0.02	0.330	±0.014	Binary	RV	[24]	
ASAS-04_P	0.8338	±0.0036	0.848	±0.005	Binary	RV	[25]	
ASAS-04_S	0.8280	±0.0040	0.833	±0.005	Binary	RV	[25]	
GJ3236_P	0.376	±0.016	0.3795	±0.0064	Binary	RV	[26]	
GJ3236_S	0.281	±0.015	0.2996	±0.0064	Binary	RV	[26]	
AP-And_P	1.211	±0.024	1.218	±0.013	Binary	RV	[27]	
AP-And_S	1.222	±0.024	1.226	±0.061	Binary	RV	[27]	
VZ-Cep_P	1.376	±0.027	1.622	±0.019	Binary	RV	[27]	
VZ-Cep_S	1.073	±0.023	0.934	±0.025	Binary	RV	[27]	
V881-Per_P	0.912	±0.039	0.975	±0.020	Binary	RV	[27]	
V881-Per_S	0.748	±0.035	0.708	±0.018	Binary	RV	[27]	

Table 2 – *continued*

Name	$M_*(M_\odot)$	$\sigma(M_*(M_\odot))$	$R_*(R_\odot)$	$\sigma(R_*(R_\odot))$	System type	Method	Ref.[a]	Comment
IM-Vir_P	0.981	±0.012	1.061	±0.016	Binary	RV	[28]	
IM-Vir_S	0.6644	±0.0048	0.681	±0.013	Binary	RV	[28]	
RXJ0239.1_P	0.730	±0.009	0.741	±0.004	Binary	RV	[29]	
RXJ0239.1_S	0.693	±0.006	0.703	±0.002	Binary	RV	[29]	
NSVS0103_P	0.5428	±0.0027	0.5260	±0.0028	Binary	RV	[30]	
NSVS0103_S	0.4982	±0.0025	0.5088	±0.0030	Binary	RV	[30]	
2MASS04463285_P	0.47	±0.05	0.56	±0.02	Binary	RV	[31]	
2MASS04463285_S	0.19	±0.02	0.21	±0.01	Binary	RV	[31]	
KIC1571511_P	1.265	$^{+0.036}_{-0.030}$	1.343	$^{+0.012}_{-0.010}$	Binary	RV	[32]	SB1
KIC1571511_S	0.141	$^{+0.005}_{-0.004}$	0.1783	$^{+0.0014}_{-0.0017}$	Binary	RV	[32]	SB1
RR-Cae	0.1825	±0.0131	0.2090	±0.0143	Binary	RV	[33]	Primary:WD
OGLE-TR-123_P	1.29	±0.26	1.55	±0.10	Binary	RV	[34]	SB1
OGLE-TR-123_S	0.085	±0.011	0.133	±0.009	Binary	RV	[34]	SB1
OGLE-TR-122_P	0.98	±0.14	1.05	$^{+0.20}_{-0.09}$	Binary	RV	[35]	SB1
OGLE-TR-122_S	0.092	±0.009	0.120	$^{+0.024}_{-0.013}$	Binary	RV	[35]	SB1
OGLE-TR-125_S	0.209	±0.033	0.211	±0.027	Binary	RV	[36]	SB1
1 OGLE-TR-120_S	0.47	±0.04	0.42	±0.02	Binary	RV	[36]	SB1
1 OGLE-TR-114_P	0.82	±0.08	0.73	±0.09	Triple	RV	[36]	
OGLE-TR-114_S	0.82	±0.08	0.72	±0.09	Triple	RV	[36]	
OGLE-TR-106_S	0.116	±0.021	0.181	±0.013	Binary	RV	[36]	SB1
1 OGLE-TR-78_S	0.243	±0.015	0.24	±0.013	Binary	RV	[36]	SB1
1 OGLE-TR-65_P	1.15	±0.03	1.58	±0.07	Triple	RV	[36]	
OGLE-TR-65_S	1.11	±0.03	1.59	±0.05	Triple	RV	[36]	
KIC7871531	0.84	±0.02	0.874	±0.008	Single	AS	[37]	
KIC8006161	1.04	±0.02	0.947	±0.007	Single	AS	[37]	
KIC8394589	0.94	±0.04	1.116	±0.019	Single	AS	[37]	
KIC8694723	0.96	±0.03	1.436	±0.024	Single	AS	[37]	
KIC8760414	0.77	±0.01	1.006	±0.004	Single	AS	[37]	
KIC9098294	1.00	±0.03	1.154	±0.009	Single	AS	[37]	
KIC9955598	0.89	±0.02	0.883	±0.008	Single	AS	[37]	

Note:[a] References: [1] Marcy et al. (2014, table 1); [2] Barclay et al. (2012, table 1); [3] Zhou et al. (2014, table 4); [4] Sandberg Lacy et al. (2014, table 7); [5] Kaluzny et al. (2013, table 12); [6] Borkovits et al. (2013, table 4); [7] Tal-Or et al. (2013, table 4); [8] Çakırlı (2013, table 5); [9] Nefs et al. (2013, table 5); [10] Carter et al. (2011, table 1); [11] Bass et al. (2012, table 6); [12] Kraus et al. (2011, table 8); [13] Parsons et al. (2012b, table 9); [14] Parsons et al. (2012a, table 5); [15] Parsons et al. (2012c, table 4); [16] Doyle et al. (2011, table 1); [17] Morales et al. (2009a, table 9); [18] Fernandez et al. (2009, table 13); [19] Beatty et al. (2007, table 8); [20] Hełminiak et al. (2012, table 5); [21] Irwin et al. (2011, table 10); [22] Birkby et al. (2012, table 11); [23] Torres et al. (2010, table 1); [24] Vaccaro et al. (2007, table 1); [25] Hełminiak & Konacki (2011, table3); [26] Irwin et al. (2009, table 9); [27] Zola et al. (2014, table 6); [28] Morales et al. (2009b, table 11); [29] López-Morales & Shaw (2007, table 2); [30] López-Morales et al. (2006, table 5); [31] Hebb et al. (2006, table 2); [32] Ofir et al. (2012, table 3); [33] Maxted et al. (2007, table 3); [34] Pont et al. (2006, table 2); [35] Pont et al. (2005a, table 2); [36] Pont et al. (2005b, table 7); [37] Metcalfe et al. (2014, table 1).

interval between 0.2 and 0.6 M$_\odot$. Y–Y models, instead, present overestimated radii only for masses below 0.45 M$_\odot$; they turn out to be underestimated instead for all higher masses. It is hard to trace back the origin of these differences.

Before exploring other possible changes to our models, we decided to look at the sequences of VLMS in open and globular clusters.

3.2 The lower MS in Praesepe

Praesepe is the perfect cluster to study the shape of the lower MS: it is reasonably well populated, it has an age high enough to have all VLMS already settled on the MS, and in addition it has excellent (and uncontroversial) trigonometric parallaxes from *Hipparcos*. van Leeuwen (2009) finds $(m - M)_0 = 6.30$ mag, $\log(\text{age/yr}) = 8.90$ ($\sim$0.8 Gyr) and $E(B - V) = 0.01$ mag. In addition, the cluster has been recently and deeply observed by the Panoramic Survey Telescope & Rapid Response System (Pan-STARRS); Wang et al. (2014) provide a comprehensive catalogue containing hundreds of

VLMS, with memberships provided by the combination of Pan-STARRS and 2MASS photometry, and PPMXL proper motions.

Fig. 3 presents the Wang et al. (2014) data in several diagrams involving Pan-STARRS and 2MASS photometry, and as compared to a few sets of models. The models are initially shown in the theoretical H–R and mass–luminosity plots (top panels), for an age of $\log(\text{age/yr}) = 8.90$ (van Leeuwen 2009) and a metallicity of $Z = 0.02$ [Carrera & Pancino (2011) present [Fe/H] = 0.16, which corresponds to $Z = 0.0244$ with their adopted solar abundance]. Then, the other panels show the $g - z$ versus z, and the $g - K_s$ and $J - K_s$ versus K_s CMDs. It is evident that the previous PARSEC v1.1 models (black and blue lines, with OBC and NBC, respectively) fail to describe the lower MS in CMDs involving the optical filters g and z. In the case of the near-infrared $J - K_s$ versus K_s CMD, the colour offset of the PARSEC v1.1 models almost completely disappears when we adopt the new BC$_\lambda$ NBC (blue lines). In all the other CMDs, using the NBC just slightly moves the VLMS models towards the observed sequence.

The use of the T–τ relation, as illustrated by the green lines, causes the optical colours to move towards the observed sequences

in a slightly more decisive way, but anyway, it is evident that no good agreement with the data is reached. The only exception seems to be the near-infrared $J - K_s$ versus K_s diagram, in which all the model sequences in which the NBC tables are used appear with satisfactory agreement with the data, being able to produce the vertical sequence observed at $J - K_s \simeq 0.9$. Possible discrepancies with the data are at a level of just a few hundredths of magnitude in $J - K_s$.

Anyway, the important point that comes out of this comparison is the incapacity of models using the T–τ relation, and the latest tables of BC$_\lambda$, to reproduce the optical colours of VLMS in Praesepe, with discrepancies being as large as ~ 1 mag in colours as $g - z$ and $g - K_s$. The models turn out to be far too blue, which suggests that some improvement could be reached by further decreasing the $T_{\rm eff}$ – hence increasing the stellar radius – of the models, as we will see later.

3.3 The lower MS in M67

The open cluster M67 constitutes another excellent testing ground for our models, since it has extensive photometric and membership data, added to well-determined global ages and metallicities (e.g. VandenBerg & Stetson 2004; Randich et al. 2006), and a small foreground reddening.

We have combined the following data sources for M67:

(i) the astrometry, *BVI* photometry and membership probability $P_{\rm mb}$ from Yadav et al. (2008);
(ii) the 2MASS very deep photometry from the 'Combined 2MASS Calibration Scan' (Cutri et al. 2003; see also section 2 of Sarajedini et al. 2009);
(iii) the SDSS point spread function photometry as performed by An et al. (2008).

The different catalogues were cross-matched with Starlink Tables Infrastructure Library Tool Set (STILTS) (Taylor 2006) revealing positional offsets typically smaller than 0.5 arcsec. Fig. 4 shows a few of the resulting CMDs for stars with $P_{\rm mb} > 20$ per cent. These diagrams are typically very clean for all magnitudes brighter than $g = 20$, whereas a significant number of outliers appear at fainter magnitudes – either due to the more uncertain memberships or to the worse photometric quality in this range of brightness. The important point for us is that the lower MS is very well delineated. A parallel sequence of nearly-equal-mass binaries is also evident, and located 0.7 mag above the MS.

In Fig. 4, we present the fit of M67 for which we assume a distance modulus $(m - M)_0 = 9.75$ mag and a reddening $E(B - V) = 0.03$ mag. For the sake of simplicity, we use models with $Z = 0.02$ and, since this value is slightly higher than the observed metallicity (Sarajedini et al. 2009), we obtain an age of 3.5 Gyr which is a lower limit to the ages quoted in the literature (Sarajedini et al. 2009). As we will see in the following, this will not affect the results of our investigation. In the H–R diagram (top-left panel of Fig. 4), these isochrones appear nearly identical to those shown for Praesepe, for all luminosities below $\sim 1\,{\rm L}_\odot$. The comparison with the models reveals essentially the same situation as for Praesepe: whereas the NBC and the use of the T–τ relations both contribute to redden the model VLMS sequences and reduce the disagreement with the data, the revised PARSEC v1.2+NBC models remain too blue at optical colours. The near-infrared colour $J - K_s$ instead is little affected by the changes in the T–τ relation and reasonably well reproduced by all the NBC models.

The comparison with the blue band colours, such as the $B - V$, is more problematic and it is discussed in detail in Appendix A.

3.4 Ultradeep *HST*/ACS data for 47 Tuc and NGC 6397

47 Tuc (NGC 104) is a relatively metal rich globular cluster. The most recent abundance determination gives [Fe/H] $= -0.79$ and a median value of [O/Fe] ~ 0.2 (Cordero et al. 2014). Carretta et al. (2010) give a distance modulus of $(m - M)_V = 13.32$, an age of 12.83 Gyr and a reddening of $E(B - V) = 0.04$ mag, while Hansen et al. (2013) determine an age of 9.7 Gyr from the white dwarf cooling sequence. Kalirai et al. (2012) obtained extremely deep *Hubble Space Telescope* (*HST*)/Advanced Camera for Surveys (ACS) *F*606*W* and *F*814*W* data for this cluster (with 50 per cent completeness limits at ~ 29.75 and 28.75 mag for *F*606*W* and *F*814*W*, respectively), which makes it an excellent test bed for the lower MS. We compare our models with these observational data in Fig. 5. To fit the data with our models, we assume a metallicity of $Z = 0.004$, a distance modulus of $(m - M)_0 = 13.20$, an age of 10 Gyr and $E(B - V) = 0.05$ mag.

It is evident that PARSEC v1.1 and v1.2 models fail to reproduce the lower MS in 47 Tuc, in a way similar to what was already noticed for Praesepe and M67. It is also evident that the NBC and the use of T–τ relations cause models to move on the right direction, but do not suffice for them to reach the observed sequences. In 47 Tuc, the discrepancy between models and data starts at about *F*814*W* $= 20$, which corresponds approximately to stellar models of mass $M = 0.6\,{\rm M}_\odot$. Finally, we note that with an isochrone of 12.6 Gyr, we can also fit the turn-off very well, while with the isochrone of 10 Gyr, we need to enhance the helium content. But since the goal of this paper is to improve the models for the lower MS, we leave the detailed modelling of the turn-off and red giant sequences to a future work.

Going to even smaller metallicities, we have the case of NGC 6397 with a measured metallicity of [Fe/H] $= -1.988$ (and [α/Fe] $= 0.36$; cf. Carretta et al. (2010), corresponding to $Z = 0.000\,376$ with their adopted solar abundance). Carretta et al. (2010) also give a distance modulus of $(m - M)_V = 12.31$, an age of 13.36 Gyr and a reddening of $E(B - V) = 0.18$ mag. Richer et al. (2008) observed this cluster with *HST*/ACS and, after proper motion cleaning, obtained a very narrow MS down to *F*814*W* ~ 26 mag, as shown in Fig. 6. To fit the data with our models, we assume a metallicity of $Z = 0.0005$ (the nearest metallicity in PARSEC v1.1), a distance modulus of $(m - M)_0 = 11.95$, an age of 12 Gyr and $E(B - V) = 0.2$ mag. Comparison with PARSEC v1.1 and v1.2 models reveals about the same discrepancies as for 47 Tuc, but now starting at *F*814*W* $\simeq 19$ mag.

We remind the reader that the models used here adopt a solar abundance partition, without enhancement of α elements. While the effect of α-enhancement is the goal of a forthcoming detailed analysis on globular clusters properties, we notice that its effects on the T–τ relation are of secondary importance, after it is accounted for in deriving the global metallicity.[8]

3.5 Comparing the CMDs with other models

The sequence of Figs 7–10 compares our best-performing isochrone set so far – namely the PARSEC v1.2+NBC – with those from other groups already introduced in Section 3.1, and with the data of the four clusters we have just discussed. In doing so, we are by no means trying to find the best-fitting isochrone for each model set

---

[8] As first noted by Kalirai et al. (2012), a dispersion in the abundance ratios might be at the origin of the colour dispersion observed at the bottom of the MS in 47 Tuc.
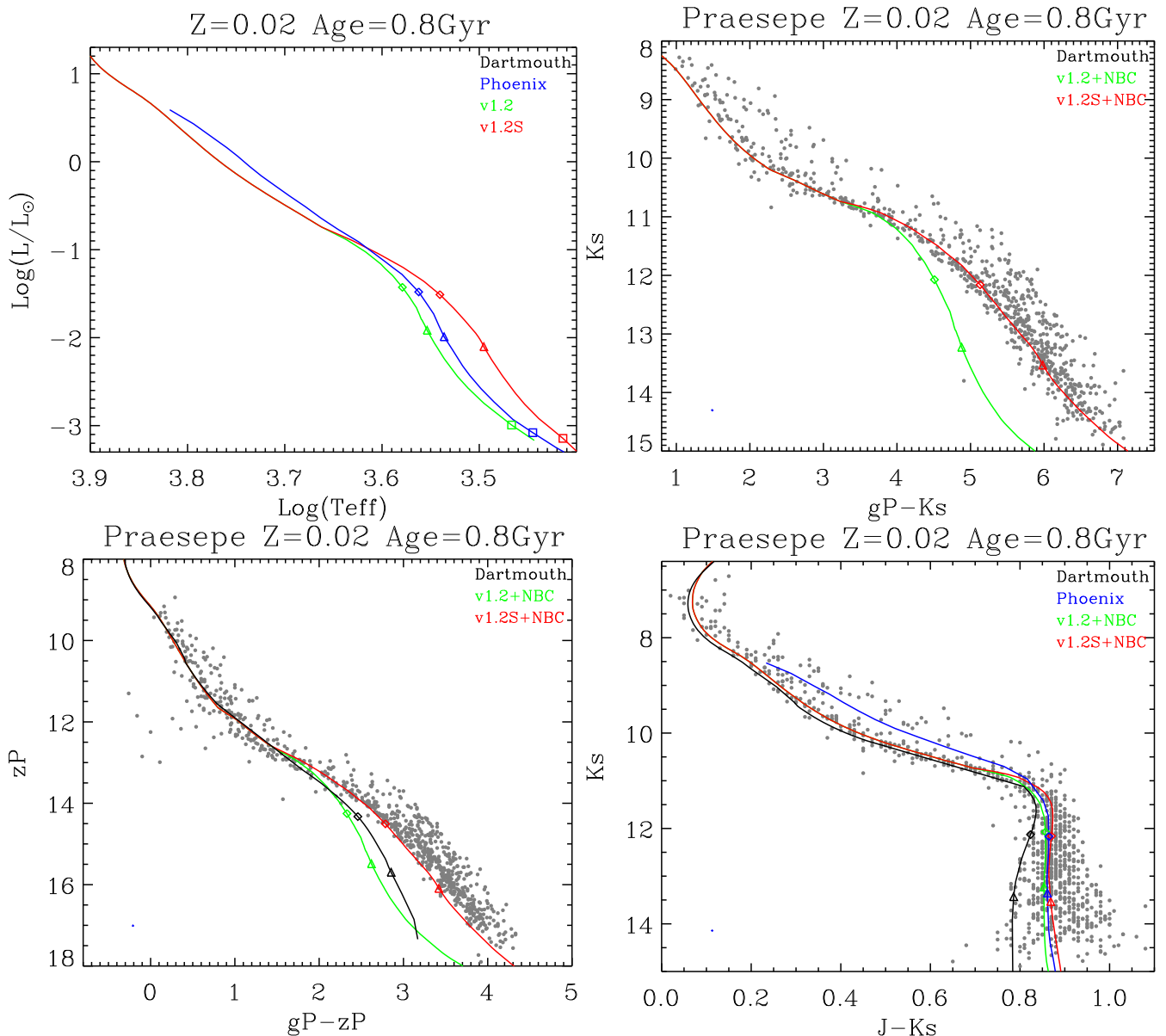
Figure 7. CMDs for Praesepe, same as in Fig. 3, except that the black lines are for Dartmouth with $Z = 0.018\,85$ and age $= 0.8$ Gyr, and the blue ones are for PHOENIX with $Z = 0.02$ and age $= 0.8$ Gyr.

and cluster, we are just overplotting them for the same assumed distance and reddening, for a quick comparison of the several sets. The comparisons are first made in the H–R diagram, and later in the CMDs for which we have isochrones available in the same filter sets.

As can be seen in the figures, none of the sets being compared agree perfectly in the H–R diagram, even if the Y–Y and Dartmouth models implement similar T–τ relations as in our PARSEC v1.2 models. Our v1.2 models are slightly hotter than both Dartmouth and PHOENIX models in the lower MS at near-solar metallicity (Figs 7 and 8), but still significantly hotter than those at low metallicities (Figs 9 and 10). Tracing back the origin of these differences is difficult at this stage, and is beyond the scope of this paper.

When we look at the CMDs in Figs 7–10, in addition to the intrinsic difference in the evolutionary tracks, we also see the effect of the different tables of BC_λ adopted by the different groups. What is more remarkable in the Preasepe and M67 plots is that all models

seem to reproduce satisfactorily the kink that occurs at the bottom of the MS in the near-infrared colour $J - K_s$. However, in all cases the fit is far from satisfactory when we look at the colours which involve optical filters. The same applies to the two old globular clusters as shown in Figs 9 and 10.

4 DISCUSSION AND CONCLUSIONS

As is evident from the previous discussion, adopting better BC tables and $T–\tau$ relations is not enough to bring models and data into agreement, and the problem seems to extend to other sets of models in the literature as well. Interestingly, we note that the changes requested in the mass–radius relation – namely larger radii at a given mass – go in the same sense of the changes required to improve the agreement with the CMDs – namely lower $T_{\rm eff}$ (larger radii) for a given luminosity. Moreover, the discrepancies start to appear more or less at the same masses down the MS, namely at $\sim$0.5 M$_\odot$.
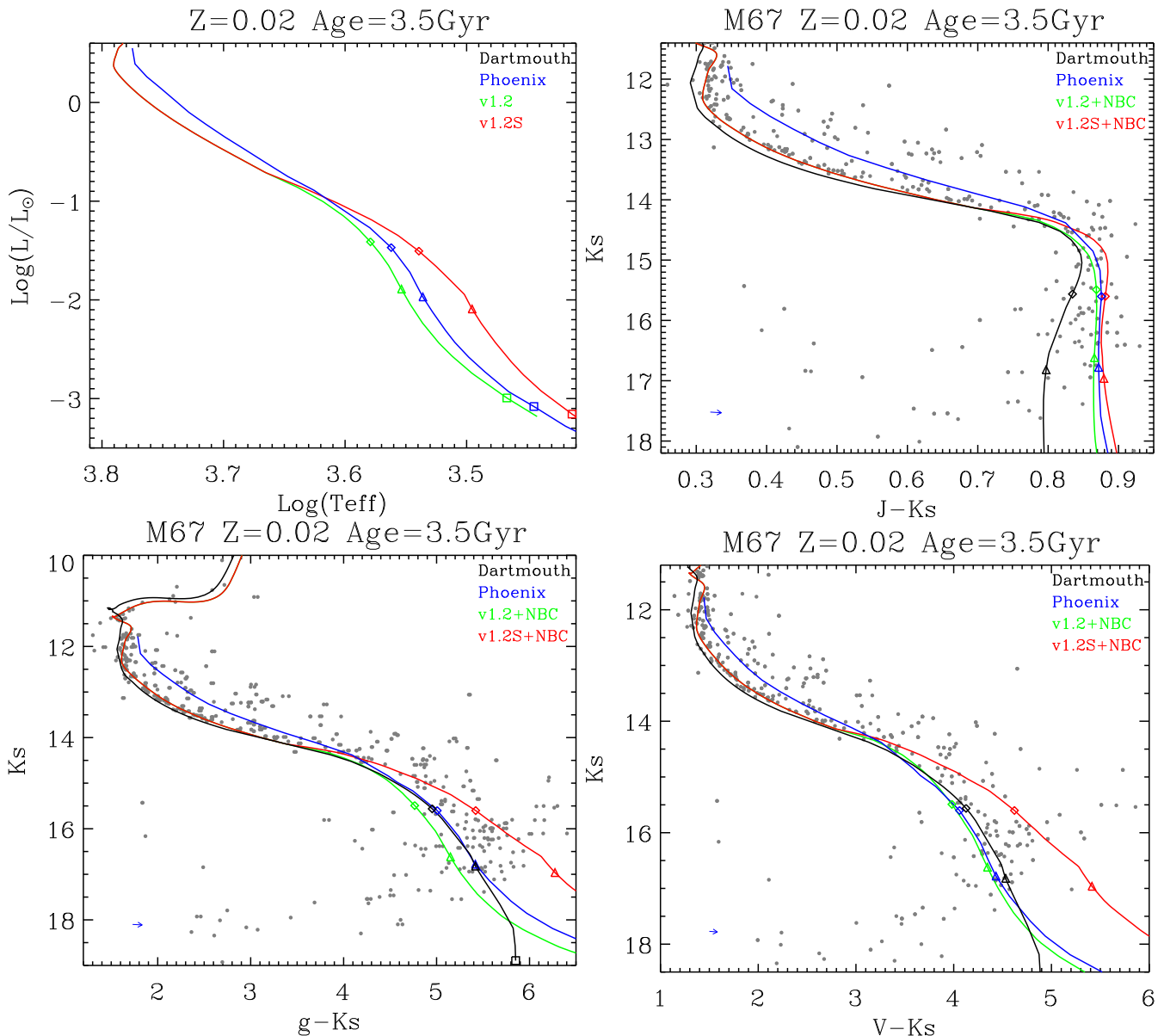
Figure 8. M67 in several CMDs, same as in Fig. 4, except that the black lines are for Dartmouth with $Z = 0.018\,85$ and age = 3.5 Gyr, and the blue ones is for PHOENIX with $Z = 0.02$ and age = 3.5 Gyr.

Therefore, it is natural to seek for changes that increase the stellar radii of the models, and check whether this causes better agreement with the CMD data. This is essentially the approach we will pursue in the following.

4.1 A recalibration of the T–τ relation

As can be seen in Fig. 1, the BT-Settl T–τ relations are distributed in a relatively narrow region of the $T/T_{\rm eff}$ versus τ plane and, at large values of τ, they converge towards and even exceed the grey T–τ relation. This effect becomes more prominent at lower effective temperatures, where the T–τ relations near the photosphere become significantly hotter than the grey atmosphere one. The excess reaches $\Delta \log(T/T_{\rm eff}) \sim 0.04$ dex and is likely caused by the formation of molecules at low temperatures, which trap the radiation in the atmosphere. It is this shift of the T–τ relation that causes some improvement in the mass–radius of the MS models

and, consequently, on the corresponding colour–magnitude relations. However, the agreement with observations of lower MS stars is far from being satisfactory. Thus, we wonder if (1) the mismatch can be due to an underestimate of the photospheric temperature by the T–τ relations at smaller $T_{\rm eff}$, and if (2) we could use the observed mass–radius relation shown in Fig. 2 to calibrate the T–τ relations at low effective temperatures.

Concerning the first point, we can only say that there are many such relations in the literature and that the empirically checked Krishna Swamy (1966) relation predicts a significant shift already at ~5000 K (dwarf stars), comparable to that obtained by the BT-Settl T–τ relation of the 2600 K model.

Concerning the second point, we have calculated a series of models for low-mass stars where we have applied a shift to the low-temperature T–τ relations, to reproduce the observed mass–radius relation. The correction factor depends on the effective temperature. It is $\Delta \log(T/T_{\rm eff}) = 0$ at $\log(T_{\rm eff}/{\rm K}) = 3.675$, and it
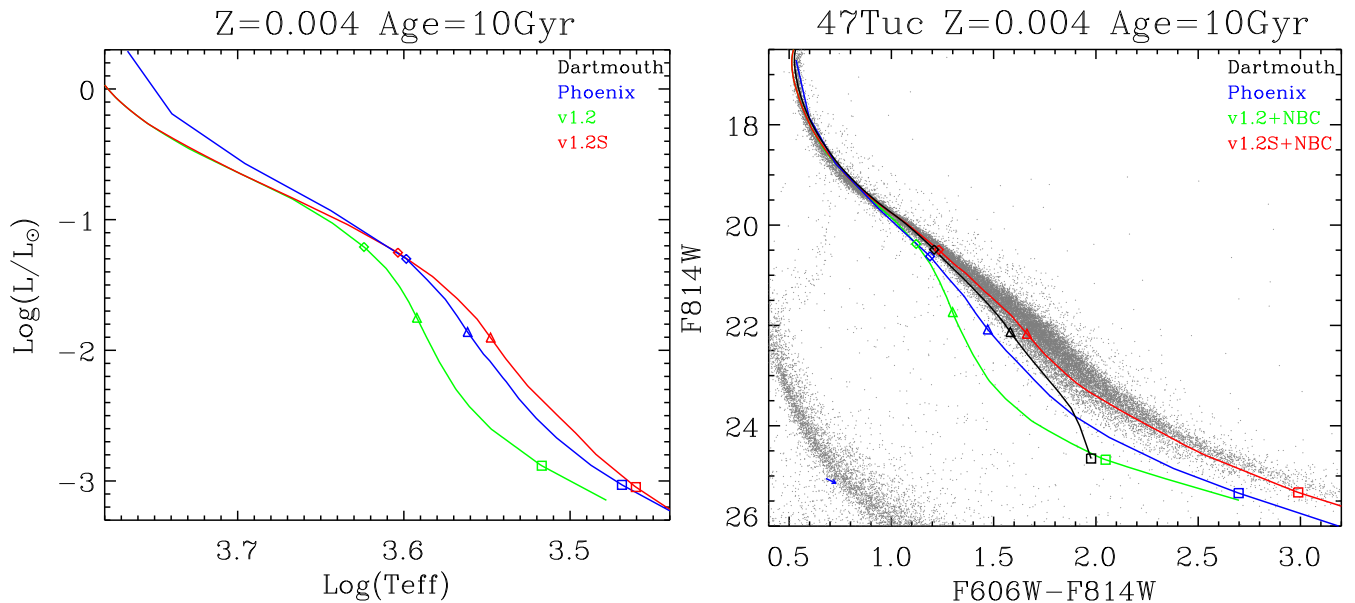
Figure 9. CMDs for 47 Tuc, same as in Fig. 5, except that black lines are for Dartmouth ($Z = 0.005\,3740$ and age = 10 Gyr) and blue ones are for PHOENIX ($Z = 0.006\,340$ and age = 10 Gyr).
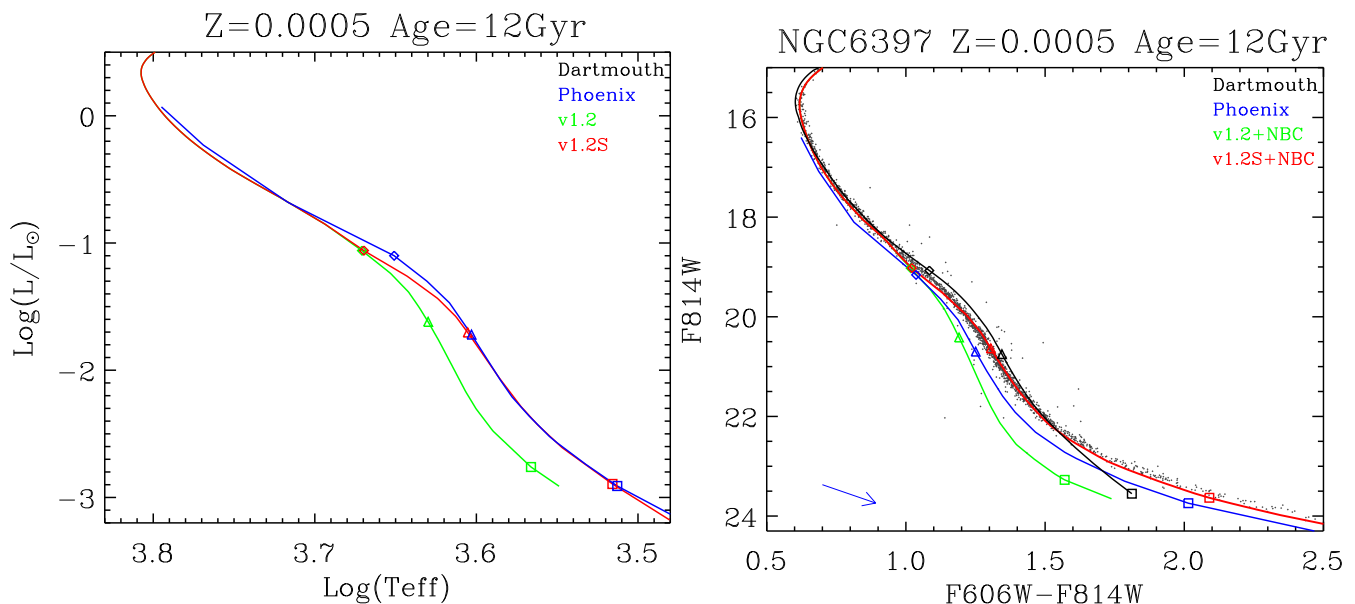

Figure 10. CMDs for NGC 6397, same as in Fig. 6, except that black lines are for Dartmouth ($Z = 0.000\,546\,51$ and age = 12 Gyr), and blue ones are for PHOENIX ($Z = 0.000\,307$ and age = 12 Gyr).

increases linearly to $\Delta\log(T/T_{\rm eff}) \sim 0.06$ dex (~ 14 per cent), at $\log(T_{\rm eff}/{\rm K}) = 3.5$. The resulting T–$\tau$ relations are shown in Fig. 11. Note that the correction is applied *only* to the T–τ relation and we use our own EOS and opacity to get the pressure structure in the atmosphere. The mass–radius calibration is shown in Fig. 12, where it is indicated as PARSEC v1.2S models. We checked that no shift is necessary at $T_{\rm eff}$ higher than $\log(T_{\rm eff}/{\rm K}) = 3.675$, since there is no need to alter the radii of stars with masses larger than $M = 0.7\,{\rm M_\odot}$ at solar metallicities.

We now look at the effects of this calibration on the colour–magnitude relations of VLMS in clusters. The results are illustrated by means of the PARSEC v1.2S+NBC models (red lines) overplotted in Figs 3, 4, 5 and 6, for Praesepe, M67, NGC 6398 and 47

Tuc, respectively. Note that the same $T_{\rm eff}$-dependent shift, obtained from the calibration with the mass–radius relation, is applied for all metallicities. Careful inspection of these plots reveals that the T–τ-calibrated models provide an excellent fit to the lower MS in all these clusters, spanning a range of ~ 2 dex in metallicity.

This result is remarkable. It is probably indicating that the problem at the origin of the too small radii in present VLMS models might be the same as that at the origin of their bad reproduction of the observed lower MS in cluster CMDs. Whether the present recipe of calibrating the available T–τ relations in the way we described is an acceptable solution is another question, which we open for discussion. Of course, we are well aware that, at this stage, this is not more than 'a recipe that works', rather than a recommendation
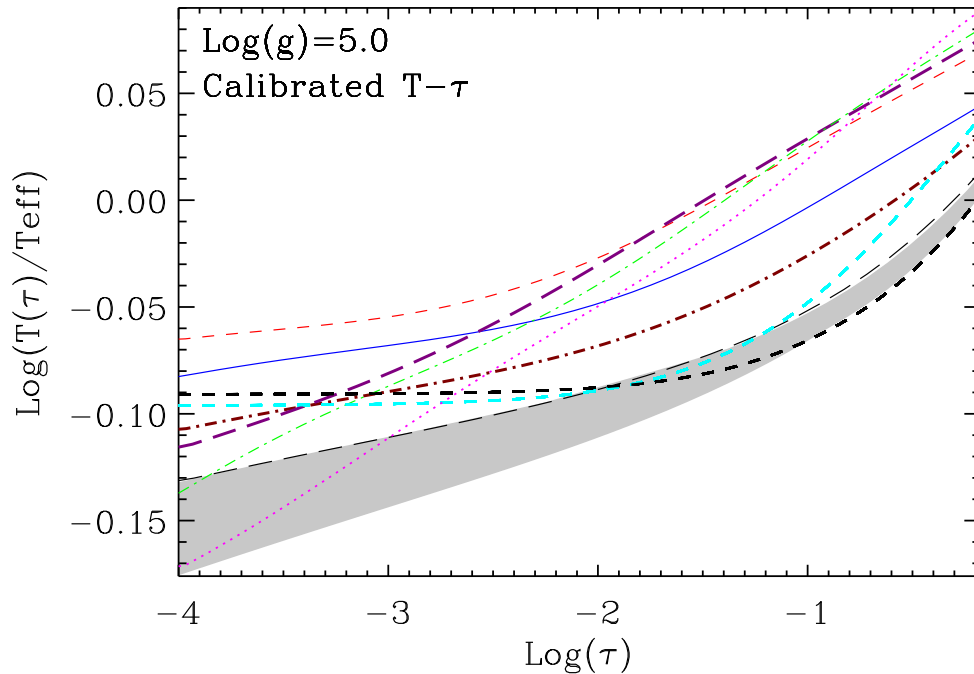
Figure 11. As Fig. 1, but for calibrated $T-\tau$ relations, as described in Section 4.1.
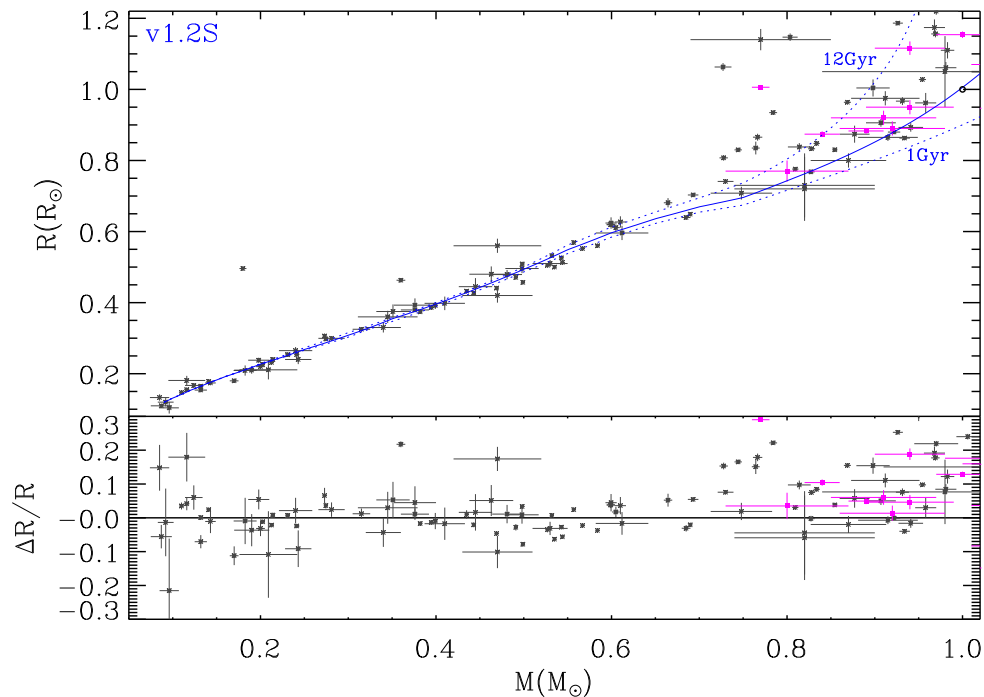

Figure 12. As Fig. 2, but for calibrated $T-\tau$ relation. We also plot isochrones with ages of 12 and 1 Gyr.

we can do to stellar modellers. Work is necessary to clarify whether more realistic descriptions of stellar atmospheres – like for instance full 3D hydrodynamical models – may lead to any indication of this kind or to alternative recipes.

Another aspect revealed by Figs 3 and 4 is that the *near-infrared* CMDs of VLMS can be reproduced fairly well with the published $T-\tau$ relations, provided that one uses the correct BC$_\lambda$. In the very low mass regime, they are not as sensitive to $T_{\rm eff}$ as the optical

CMDs. Indeed, we emphasize that the optical CMDs should be considered as stronger diagnostic tools, together with the mass–radius relation which we used for the final calibration. However we stress that, since the relation between mass and near-infrared luminosity is also affected by the adopted $T-\tau$ relation (see the top-left panel of Fig. 3), the use of different models, although reproducing equally well the near-infrared CMDs, may lead to different estimates of the present-day mass function in star clusters.

4.2 Data release

The VLMS models presented in this paper for $M < 0.75$ M$_\odot$ turn out to represent a significant improvement over the previous versions. The v1.2, by using a more realistic T–τ relation, clearly goes in the direction of presenting larger radii and cooler T_{eff}, which is indicated by the data. Moreover, the 'calibrated' v1.2S models fit very well the mass–radius and CMD data of VLMS in the solar neighbourhood and in star clusters over a wide range of metallicities, hence representing a good alternative to be applied in a series of astrophysical problems, going from the derivation of parameters of star clusters and transiting planets to the interpretation of star counts in the Galaxy in terms of both their mass function and density variations across the galactic disc and halo.

Therefore, we are releasing these two new sets of evolutionary tracks through our web servers at http://stev.oapd.inaf.it. These VLMS models replace those in the previous data base of PAR-SEC isochrones (namely v1.1; Bressan et al. 2012), producing the isochrones' version v1.2 and v1.2S. They become available using both the previous BC tables (OBC) and the revision based on BT-Settl models (NBC), for a wide variety of photometric systems, through our web interface http://stev.oapd.inaf.it/cmd. The models available are summarized in Table 1.

Forthcoming papers will further extend these models towards higher masses and other chemical mixtures, including the α-enhanced ones. Moreover, work is ongoing to further improve the BC tables, especially for the coolest stars.

ACKNOWLEDGEMENTS

REFERENCES

Allard F., Hauschildt P. H., 1995, ApJ, 445, 433
Allard F., Hauschildt P. H., Alexander D. R., Starrfield S., 1997, ARA&A, 35, 137
Allard F., Hauschildt P. H., Alexander D. R., Ferguson J. W., Tamanai A., 2000, in Griffith C. A., Marley M. S., eds, ASP Conf. Ser. Vol. 212, From Giant Planets to Cool Stars. Astron. Soc. Pac., San Francisco, p. 127
Allard F., Homeier D., Freytag B., 2012, Phil. Trans. R. Soc. A, 370, 2765
An D. et al., 2008, ApJS, 179, 326

Arnaboldi M. et al., 2012, The Messenger, 149, 7
Asplund M., Grevesse N., Sauval A. J., Scott P., 2009, ARA&A, 47, 481
Baraffe I., Chabrier G., Allard F., Hauschildt P. H., 1997, A&A, 327, 1054
Baraffe I., Chabrier G., Allard F., Hauschildt P. H., 1998, A&A, 337, 403
Barclay T. et al., 2012, ApJ, 761, 53
Bass G., Orosz J. A., Welsh W. F., Windmiller G., Ames Gregg T., Fetherolf T., Wade R. A., Quinn S. N., 2012, ApJ, 761, 157
Basu S., Chaplin W. J., Elsworth Y., New R., Serenelli A. M., 2009, ApJ, 699, 1403
Beatty T. G. et al., 2007, ApJ, 663, 573
Bertelli G., Girardi L., Marigo P., Nasi E., 2008, A&A, 484, 815
Bessel M. S., 1990, A&AS, 83, 357
Bessel M. S., 1990, PASP, 102, 1181
Birkby J. et al., 2012, MNRAS, 426, 1507
Böhm-Vitense E., 1958, Z. Astrophys., 46, 108
Borkovits T. et al., 2013, MNRAS, 428, 1656
Borucki W. J. et al., 2011, ApJ, 736, 19
Boyajian T. S. et al., 2012, ApJ, 757, 112
Bressan A., Marigo P., Girardi L., Salasnich B., Dal Cero C., Rubele S., Nanni A., 2012, MNRAS, 427, 127
Bressan A. G., Chiosi C., Bertelli G., 1981, A&A, 102, 25
Çakırlı Ö., 2013, New Astron., 22, 15
Caffau E., Ludwig H., Steffen M., Ayres T. R., Bonifacio P., Cayrel R., Freytag B., Plez B., 2008, A&A, 488, 1031
Caffau E., Maiorca E., Bonifacio P., Faraggiana R., Steffen M., Ludwig H., Kamp I., Busso M., 2009, A&A, 498, 877
Campos F., Kepler S. O., Bonatto C., Ducati J. R., 2013, MNRAS, 433, 243
Carrera R., Pancino E., 2011, A&A, 535, A30
Carretta E., Bragaglia A., Gratton R. G., Recio-Blanco A., Lucatello S., D'Orazi V., Cassisi S., 2010, A&A, 516, A55
Carter J. A. et al., 2011, Science, 331, 562
Casagrande L., Flynn C., Bessell M., 2008, MNRAS, 389, 585
Castelli F., Kurucz R. L., 2003, in Piskunov N., Weiss W. W., Gray D. F., eds, Proc. IAU Symp. 210, Modelling of Stellar Atmospheres. Astron. Soc. Pac., San Francisco, p. 20
Chabrier G., 2001, ApJ, 554, 1274
Copeland H., Jensen J. O., Jorgensen H. E., 1970, A&A, 5, 12
Cordero M. J., Pilachowski C. A., Johnson C. I., McDonald I., Zijlstra A. A., Simmerer J., 2014, ApJ, 780, 94
Cutri R. M. et al. eds, 2003, 2MASS All Sky Catalog, NASA/IPAC Infrared Science Archive, available at: http://irsa.ipac.caltech.edu/applications/Gator/
Cyburt R. H. et al., 2010, ApJS, 189, 240
Dahn C. C. et al., 2002, AJ, 124, 1170
Dotter A., Chaboyer B., Jevremović D., Kostov V., Baron E., Ferguson J. W., 2008, ApJS, 178, 89
Doyle L. R. et al., 2011, Science, 333, 1602
Eker Z., Bilir S., Soydugan F., Yaz Gokce E., Soydugan E., Tuysuz M., Senyuz T., Demircan O., 2014, PASA, 31, 24 E
Feiden G. A., Chaboyer B., 2012, ApJ, 757, 42
Feiden G. A., Chaboyer B., 2013, ApJ, 779, 183
Fernandez J. M. et al., 2009, ApJ, 701, 764
Girardi L., Bressan A., Bertelli G., Chiosi C., 2000, A&AS, 141, 371
Girardi L., Bertelli G., Bressan A., Chiosi C., Groenewegen M. A. T., Marigo P., Salasnich B., Weiss A., 2002, A&A, 391, 195
Green G. M. et al., 2014, ApJ, 783, 114
Hansen B. M. S. et al., 2013, Nature, 500, 51
Hebb L., Wyse R. F. G., Gilmore G., Holtzman J., 2006, AJ, 131, 555
Hełminiak K. G., Konacki M., 2011, A&A, 526, A29
Hełminiak K. G. et al., 2012, MNRAS, 425, 1245
Henyey L. G., Forbes J. E., Gould N. L., 1964, ApJ, 139, 306
Hofmeister E., Kippenhahn R., Weigert A., 1964, Z. Astrophys., 59, 215
Iglesias C. A., Rogers F. J., 1996, ApJ, 464, 943
Irwin J. et al., 2009, ApJ, 701, 1436
Irwin J. M. et al., 2011, ApJ, 742, 123
Ivezić Ž., Beers T. C., Jurić M., 2012, ARA&A, 50, 251
Jackson R. J., Jeffries R. D., 2014, MNRAS, 441, 2111
Jurić M. et al., 2008, ApJ, 673, 864

Kalirai J. S. et al., 2012, AJ, 143, 11
Kaluzny J. et al., 2013, AJ, 145, 43
Kippenhahn R., Weigert A., Weiss A., 2013, Stellar Structure and Evolution. Springer, Berlin
Kraus A. L., Tucker R. A., Thompson M. I., Craine E. R., Hillenbrand L. A., 2011, ApJ, 728, 48
Krishna Swamy K. S., 1966, ApJ, 145, 174
Kroupa P., 2001, MNRAS, 322, 231
Lawrence A. et al., 2007, MNRAS, 379, 1599
Leggett S. K., 1992, ApJS, 82, 351
López-Morales M., Orosz J. A., Shaw J. S., Havelka L., Arevalo M. J., McIntyre T., Lazaro C., 2006, preprint (astro-ph/0610225)
López-Morales M., Shaw J. S., 2007, in Kang Y. W., Lee H.-W., Leung K.-C., Cheng K.-S., eds, ASP Conf. Ser. Vol. 362, The Seventh Pacific Rim Conference on Stellar Astrophysics. Astron. Soc. Pac., San Francisco, p. 26
MacDonald J., Mullan D. J., 2013, ApJ, 765, 126
Marcy G. W. et al., 2014, ApJS, 210, 20
Marigo P., Aringer B., 2009, A&A, 508, 1539
Maxted P. F. L., O'Donoghue D., Morales-Rueda L., Napiwotzki R., Smalley B., 2007, MNRAS, 376, 919
Metcalfe T. et al., 2014, preprint (arXiv:1402.3614)
Mihalas D., 1978, Stellar Atmospheres, 2nd edn. Freeman & Co., San Francisco
Mihalas D., Hummer D. G., Mihalas B. W., Daeppen W., 1990, ApJ, 350, 300
Morales J. C. et al., 2009a, ApJ, 691, 1400
Morales J. C., Torres G., Marschall L. A., Brehm W., 2009b, ApJ, 707, 671
Nefs S. V. et al., 2013, MNRAS, 431, 3240
Nikolaev S., Weinberg M. D., 2000, ApJ, 542, 804
Ofir A., Gandolfi D., Buchhave L., Lacy C. H. S., Hatzes A. P., Fridlund M., 2012, MNRAS, 423, L1
Parsons S. G. et al., 2012a, MNRAS, 419, 304
Parsons S. G. et al., 2012b, MNRAS, 420, 3281
Parsons S. G. et al., 2012c, MNRAS, 426, 1950
Pont F., Melo C. H. F., Bouchy F., Udry S., Queloz D., Mayor M., Santos N. C., 2005a, A&A, 433, L21
Pont F., Bouchy F., Melo C., Santos N. C., Mayor M., Queloz D., Udry S., 2005b, A&A, 438, 1123
Pont F. et al., 2006, A&A, 447, 1035
Quintana E. V. et al., 2014, Science, 344, 277
Rajpurohit A. S., Reylé C., Allard F., Homeier D., Schultheis M., Bessell M. S., Robin A. C., 2013, A&A, 556, A15
Randich S., Sestito P., Primas F., Pallavicini R., Pasquini L., 2006, A&A, 450, 557
Richer H. B. et al., 2008, AJ, 135, 2141
Rogers F. J., Swenson F. J., Iglesias C. A., 1996, ApJ, 456, 902
Sandberg Lacy C. H., Torres G., Wolf M., Burks C. L., 2014, AJ, 147, 1
Sandquist E. L., 2004, MNRAS, 347, 101
Sarajedini A., Dotter A., Kirkpatrick A., 2009, ApJ, 698, 1872
Siegel M. H., Majewski S. R., Reid I. N., Thompson I. B., 2002, ApJ, 578, 151
Skrutskie M. F. et al., 2006, AJ, 131, 1163
Spada F., Demarque P., Kim Y.-C., Sills A., 2013, ApJ, 776, 87
Spruit H. C., Weiss A., 1986, A&A, 166, 167
Tal-Or L. et al., 2013, A&A, 553, A30
Taylor M. B., 2006, in Gabriel C., Arviset C., Ponz D., Enrique S., eds, ASP Conf. Ser. Vol. 351, Astronomical Data Analysis Software and Systems XV. Astron. Soc. Pac., San Francisco, p. 666
Torres G., Andersen J., Giménez A., 2010, A&AR, 18, 67
Vaccaro T. R., Rudkin M., Kawka A., Vennes S., Oswalt T. D., Silver I., Wood M., Smith J. A., 2007, ApJ, 661, 1112
van Leeuwen F., 2009, A&A, 497, 209
VandenBerg D. A., Stetson P. B., 2004, PASP, 116, 997
VandenBerg D. A., Edvardsson B., Eriksson K., Gustafsson B., 2008, ApJ, 675, 746
Wang P. F. et al., 2014, ApJ, 784, 57
Wright E. L. et al., 2010, AJ, 140, 1868
Yadav R. K. S. et al., 2008, A&A, 484, 609
Zasowski G. et al., 2013, AJ, 146, 81
Zhou G. et al., 2014, MNRAS, 437, 2831
Zola S., Şenavcı H. V., Liakos A., Nelson R. H., Zakrzewski B., 2014, MNRAS, 437, 3718

APPENDIX A: BLUE BAND COLOURS

As already discussed, we were able to obtain new stellar evolution models of low-mass stars that can reproduce fairly well the observed MS of star clusters in a broad range of ages and metallicities. We show here that there remains some tension when we try to reproduce the optical colours, such as $B - V$, of selected nearby clusters, and discuss the possible origin of the remaining discrepancies.

In Fig. A1, we compare our models with one of the deepest CMD of M67 in the V versus $B - V$ diagram (Yadav et al. 2008). The models plotted are the same as used in Fig. 4 and show the following characteristics. First of all, they are able to reproduce the MS down to about 3 mag below the turn-off, but then they run bluer than the observed data at fainter magnitudes. It is also evident that the major difference between the models is due to the use of revised BC_λ rather than to the $T-\tau$ relation. The discrepancy with the data reaches $\delta(B - V) = 0.4$ at $V = 19$, even if our new models perform very well in other colours for the same cluster (as seen in Fig. 4).
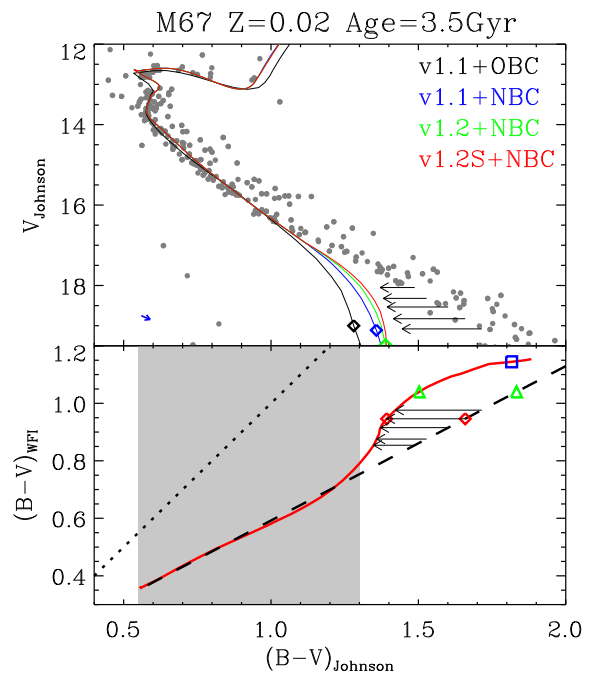

Figure A1. Top panel: the M67 data from Yadav et al. (2008), in the V versus $B - V$ diagram (grey dots). These data were originally collected in the ESO/WFI filters and then transformed to a Johnson system (see the text). Our isochrones in the Johnson system are overlaid, using the same labels and parameters as in Fig. 4. Bottom panel: the difference between ESO/WFI $B - V$ and Johnson $B - V$, with our v1.2S isochrone shown as a red solid line. The black dashed line represents the linear transformation between these two systems as defined in the colour range of $0.55 < (B - V)_{\rm Johnson} < 1.3$ (grey shaded region) and extrapolated to redder colour (or lower masses). The horizontal black arrows indicate the corrections that should have been applied to the linear transformation, in order to more correctly represent the colours of the redder stars observed with ESO/WFI filters. The dotted line is the identity line.

To find the origin of this large discrepancy, we first remind the reader that Yadav et al. (2008)'s data were obtained using a far-from-standard *B* filter, namely the ESO#842 filter available at the ESO/Wide Field Imager (WFI) camera in 2000. This *B* filter has a transmission curve strongly skewed towards the red and with a sharp cut-off at $\lambda > 5100$ Å, instead of the more extended (and slightly skewed to the blue) curve expected from a Johnson filter[9]. Indeed, the ESO#842 mean wavelength is close to 4637 Å, as compared to the 4460 Å of the Bessell (1990) *B* filter. When coupled to a *V* filter (with a mean wavelength of 5500 Å), ESO#842 provides a wavelength baseline of just 863 Å, as compared to the ∼1040 Å baseline expected from Johnson filters.[10]

Although collected in this very particular set of filters, Yadav et al. (2008) observations were then 'calibrated' using linear transformations between their instrumental magnitudes and the magnitudes of stars in common with the Sandquist (2004) M67 catalogue, being the latter in a well-calibrated Johnson system. As Yadav et al. (2008) show in their paper, the stars used to derive the transformations are bluer than $(B - V)_{\mathrm{Johnson}} = 1.4$ so that for redder (and fainter) stars this linear transformation becomes an extrapolation. This step is critical for obtaining reliable magnitudes of the fainter stars and its validity must be carefully assessed – especially in this case, where the *B* filter is very different from a Johnson one.

To clarify this point, we show the transformation between the ESO/WFI $B - V$ and Johnson's $B - V$ [hereafter $(B - V)_{\mathrm{WFI}}$ and $(B - V)_{\mathrm{Johnson}}$, respectively] by the red thick line in the lower panel of Fig. A1. The colours in both systems were obtained using the ZAMS of our theoretical isochrones as a baseline, together with the PHOENIX BT-Settl spectral library and the corresponding filter transmission curves. Even if it is not exactly the same method used by Yadav et al. (2008), this procedure shows that the transformation between the two photometric systems is far from being linear just redwards of $(B - V)_{\mathrm{Johnson}} = 1.3$. The analogue of the linear transformation used by Yadav et al. (2008) is shown as a dashed line in the lower panel of the same figure. The dashed line is a linear fit of the actual transformation for $(B - V)_{\mathrm{Johnson}} \geq 1.3$. We evince from this exercise that, by extrapolating the linear transformation to stars redder than $(B - V)_{\mathrm{Johnson}} = 1.3$, one gets $(B - V)_{\mathrm{Johnson}}$ colours that are significantly redder than those expected from the actual transformation. A measure of the possible error in the $(B - V)_{\mathrm{Johnson}}$ colours of VLMS is shown by the horizontal arrows in the lower panel, which are also reported in the upper panel.

These comparisons with Yadav et al. (2008) data just emphasize the need of collecting data for VLMS in nearby open clusters using *standard* filters, together with a robust calibration of the photometry based on standard stars covering the widest possible colour range. Otherwise, any comparison with theoretical models
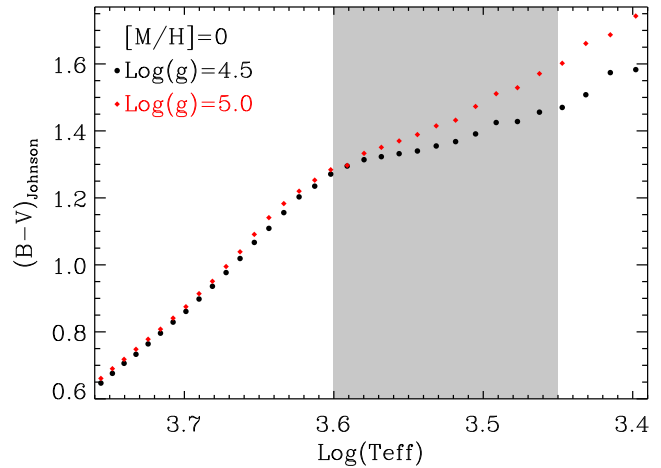

Figure A2. Temperature scale (log T_{eff} versus $(B - V)_{\mathrm{Johnson}}$) for PHOENIX BT-Settl models of $[M/H] = 0$. Red and black dots are for log $g = 5.0$ and 4.5, respectively. The grey area indicates the region where $B - V$ increases slowly as log T_{eff} decreases.

(as those presented in fig. 10 of Yadav et al. 2008) may turn out to be misleading.

To reinforce this finding, we plot in Fig. A2 the $(B - V)_{\mathrm{Johnson}}$ colours against log T_{eff} of PHOENIX models (from their website). Since below $T_{\mathrm{eff}} \simeq 4000$ K, the $B - V$ colours become quite flat, we expect a knee-like shape in the *V* versus $B - V$ diagram, as seen in our plotted isochrones, but not in the 'putative Johnson' CMD from Yadav et al. (2008).

Another interesting – and more conclusive – comparison between models and data can be done using the solar neighbourhood data compiled by I. Neill Reid from Bessel (1990), Leggett (1992) and Dahn et al. (2002) catalogues.[11] The *V* versus $B - V$ data in the Bessell system are plotted in the left-hand panel of Fig. A3, together with our models. We first notice that these data show the expected knee-like shape in the very low mass range. But we also notice that our best model mismatch the data by ∼0.1 mag at 0.3 M$_\odot$. We suspect that this discrepancy originates from some molecular absorption bands around 4400 Å (AlH and NaH) being still unaccounted for in the models, as recently pointed out in Rajpurohit et al. (2013). Indeed, from their fig. 3, we notice that the observed spectra run slightly below the PHOENIX models at ∼4400 Å in the temperature range $3000 < T_{\mathrm{eff}}/\mathrm{K} < 3700$. This shows that the real $B - V$ should be slightly redder than those obtained by the PHOENIX models, but more work is needed to check if the difference really amounts to ∼0.04 dex in flux, as expected from the observed mismatch.

Finally, the solar neighbourhood *V* versus $U - V$ data in the Bessell system are plotted in the right-hand panel of Fig. A3, together with our models. In contrast to the $B - V$ colour, our new models can fit quite well the $U - V$ knee-like shape at $U - V \simeq 2.7$, starting at $M_V \gtrsim 8$ and extending down to $M_V \simeq 11$. There remains some possible mismatch at still fainter magnitudes, but the data are too scarce for drawing definitive conclusions.
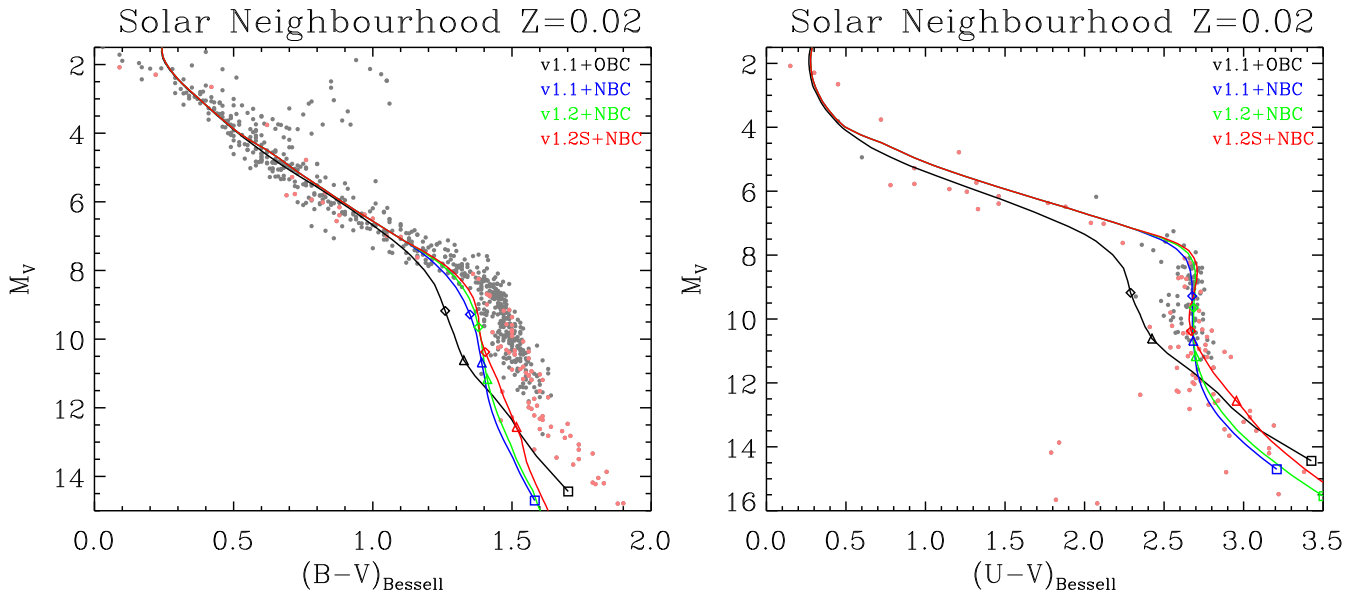
---

[9] This difference can be appreciated in fig. 3 of Girardi et al. (2002), where ESO#842 appears as the *B* filter in the ESO Imaging Survey (EIS) photometric system, and is compared to the Bessell (1990) representation of the Johnson *B* filter.

[10] These and other mean wavelengths are provided at the web interface http://stev.oapd.inaf.it/cmd, together with the theoretical isochrones.

[11] http://www.stsci.edu/inr/cmd.html

Figure A3. Solar neighbourhood stars in the M_V versus $B - V$ and M_V versus $U - V$ diagrams. The data points are from the CNS3 star sample; stars within 8 pc of the Sun are marked with pink dots. The labels are the same as in Fig. 3. The absolute magnitudes are in the Bessell photometric system (Bessell 1990). The galactic reddening is not considered in this plot. The isochrones are for $Z = 0.02$. Although the stars have different ages, their evolution is quite slow, thereby we only show the isochrones of 1 Gyr.

This paper has been typeset from a TEX/LATEX file prepared by the author.